



**Politecnico
di Torino**



POLITECNICO DI TORINO

Corso di Laurea Magistrale in Ingegneria Aerospaziale

Aeroacoustic Analysis of a Cavity Flow

Supervisors

Prof. Gioacchino CAFIERO
Prof. Francesco AVALLONE

Company Tutor

Ing. Davide MUFFO

Candidate

Gianvito POSSIDENTE

December 2024



Abstract

The study of airflow over open cavities is fundamental to the design of modern aircraft, both in civil and military aviation. Such flow is inherently unstable and leads to pressure oscillations, including broadband components and periodic tonal components, which can interfere with the aerodynamics of the aircraft. Therefore, such cavities have been investigated since the 1950s.

Rossiter was the first to describe the phenomenon, identifying the cause of the tonal pressure oscillations (which will later be called Rossiter modes) and deriving an empirical formula for their frequency, which will later be refined by Heller. Subsequent studies have discovered the existence of cavities in which the periodic pressure components are reduced, if not completely absent, and identified other parameters that influence the flow behaviour, such as the cavity length-to-depth, length-to-width and width-to-depth ratios, and the Reynolds and Mach numbers. The development of subsequent CFD techniques has allowed a greater understanding of the phenomenon, although, due to the high Reynolds numbers, the simulation of transonic and supersonic cavities remains a challenge.

In this paper, a reference geometry has been analysed through the commercial software Simulia PowerFLOW[®], which implements the Lattice-Boltzmann Method, describing how the simulation was prepared and comparing the results with those obtained experimentally and present in the literature.

Contents

1	Introduction	1
1.1	Description of Pressure Oscillations	1
1.2	Brief History of Studies about Cavity Flows	4
1.3	Aim of this Work	8
2	The Lattice-Boltzmann Method and the PowerFLOW Software	9
2.1	The Boltzmann Equation	11
2.2	The Lattice-Boltzmann Equation	13
2.3	Computational Algorithm	15
2.4	PowerFLOW Software	17
2.5	Relation with Navier-Stokes Equations	19
3	A Case of Study: the M219 Cavity	25
3.1	Case Preparation	26
3.2	Simulation	29
3.3	Results Analysis	32
4	Summary	53
	Bibliography	55
	Acronyms	57

CONTENTS

List of Figures

1.1	Two different types of cavity flow	2
1.2	Simplified model of flow over cavity	3
1.3	Boundaries of cavity flow regimes	6
2.1	Two different velocity models	14
2.2	Schematization of the algorithm steps	16
2.3	Example of boundary conditions in a D2Q9 model	17
2.4	PowerFLOW lattice elements	18
2.5	Lattice refinement example	18
3.1	M219 Cavity	25
3.2	Wind tunnel dimensions	26
3.3	Coordinate System	27
3.4	VR Regions	28
3.5	Mean pressure vs time	30
3.6	HPC <i>Legion</i> server technical specifications	31
3.7	Streamwise velocity evolution	33
3.8	Streamlines in a mid-span plane superimposed over the vorticity field	34
3.9	Vorticity evolution in a mid-span plane	35
3.10	Streamlines in a mid-span plane superimposed over the mean stream- wise velocity	36
3.11	Mean streamwise velocity profiles for different positions	37
3.12	Mean streamwise velocity and variance of velocity components in a mid-span plane	38
3.13	<i>TKE</i> for different positions	39
3.14	Boundary layer and reverse flow region comparison	40
3.15	Static pressure for three different y-normal planes	41
3.16	Streamwise velocities for three different y-normal planes	42
3.17	Mean spanwise velocity in a mid-span plane	43
3.18	Mean vertical velocity for three different y-normal planes	44
3.19	Variance of streamwise velocity for three different y-normal planes .	45

LIST OF FIGURES

3.20	Variance of vertical velocity for three different y-normal planes . . .	46
3.21	U , W , p and TKE comparison between three planes	47
3.22	OASPL with different grid resolution	48
3.23	SPL with different grid resolution	49
3.24	SPL with different numerical methods	50
3.25	OASPL with different numerical methods	51

Chapter 1

Introduction

The study of airflow over open cavities is crucial for the design of modern aircraft, in both civil and military aviation. Cavity flows, such as those over weapon bays, landing gear bays, and every opening in the airframe, are indeed widespread in current aerospace applications. Flow over such cavities is inherently unsteady and leads to pressure oscillations, which can interfere with aircraft aerodynamics and internal noise levels. Furthermore, pressure oscillations may affect structural integrity by coupling with the main flexural modes of the airframe and provoking structural failure due to acoustic fatigue. In addition, protracted vibrations may exceed the certification limit. Therefore, such cavities have been the subject of investigation since the 1950s[8, 15], both experimentally and numerically. The primary focus has been on rectangular cavities, due to their simple geometry and numerous applications.

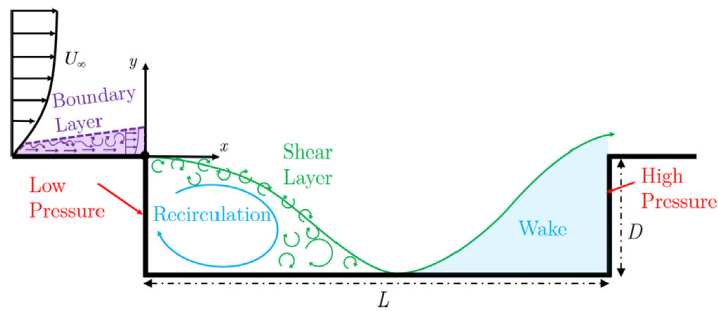
1.1 Description of Pressure Oscillations

Pressure oscillations include broadband components and periodic tonal components. The cause of the latter ones is an acoustic feedback inside the cavity: Kelvin-Helmholtz instabilities within the shear layer impinge on the downstream lip of the cavity and generate acoustic waves that propagate upstream and trigger the formation of vortices (Figure 1.1). These vortical structures interact with the same acoustic waves, generating a closed-loop feedback. These periodic fluctuations are referred to as Rossiter modes.

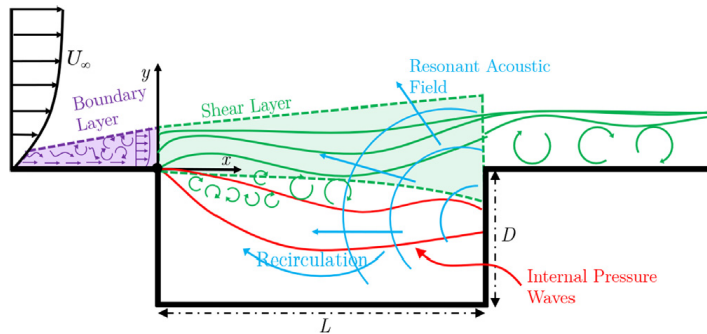
The aforementioned mechanism is true for Mach numbers lower than 2, while the cause of the pressure oscillations at higher Mach numbers is not yet known and several hypotheses have been proposed[10].

Length-to-depth and width-to-depth ratios

An important role is played by the cavity length-to-depth ratio[15]. In shallower cavities, the flow separates from the front edge and reattaches along the cavity floor (Figure 1.1a). Its pressure decreases initially, as speed increases, but then rises at the reattachment point. Approaching the downstream wall, flow pressure increases again until the boundary layer separates once more, reattaching downstream of the cavity[16]. This results in a reduction or even a total inhibition of the feedback mechanism responsible for the tonal components of pressure oscillations[10]. Hence, for higher length-to-depth ratios, random pressure oscillations are dominant. These are known as *closed cavity flows*.



(a) Closed cavity flow



(b) Open cavity flow

Figure 1.1: Two different types of cavity flow.[3]

On the other hand, as the cavity depth increases, the separation and reattachment points become closer until the two coincide, and a reverse flow between the high and low pressure regions is formed (Figure 1.1b). Thus, for deeper cavities, there are strong tonal components of pressure oscillations. These are known as *open cavity flows*.

For very high depths, the pressure spectrum presents one peak that is much larger than the others, while for lower-depth cavities there are two or more peaks

A Rossiter frequencies formula

A formula for Rossiter modes frequencies can be derived by assuming that the acoustic waves in the cavity and the vortex shedding have the same frequency. This is reasonable since the acoustic radiation excites the vortex shedding. If we consider a vortex propagation velocity equal to k_v times the free stream velocity and a sound speed inside the cavity a_c , we can say that:

$$f = \frac{k_v U_\infty}{\lambda_v} = \frac{a_c}{\lambda_a} \quad (1.1)$$

Consider an acoustic wave leaving the rear lip at $t = 0$, when a vortex is located $\gamma_v \lambda_v$ downstream of the cavity. At time $t = t'$, another sound wave reaches the cavity front lip when a vortex is shed. Assuming a number of complete wavelengths m_a involved (see Figure 1.2a), it can be stated that:

$$L = m_a \lambda_a + a_c t' \quad (1.2)$$

In the same time interval, the vortex downstream of the cavity has spaced a distance $k_v U_\infty t'$. Considering, in a similar manner, m_v complete wavelengths (see Figure 1.2b), we have:

$$m_v \lambda_v = L + \gamma_v \lambda_v + k_v U_\infty t' \quad (1.3)$$

By taking t' from one equation and substituting it into the other, and making explicit λ_a and λ_v as a function of f according to the (1.1), we obtain:

$$f = \frac{U_\infty}{L} \cdot \frac{m_a + m_v - \gamma_v}{M \frac{a_\infty}{a_c} + \frac{1}{k_v}} \quad (1.4)$$

1.2 Brief History of Studies about Cavity Flows

Early studies on cavity flows witnessed the presence of self-sustained oscillations and acoustic tones[8], but it was only Rossiter in the 1960s[16] who first described the phenomenon behind the tones and derived, empirically, a formula for the periodic components of pressure fluctuations:

$$f_m = \frac{U_\infty}{L} \cdot \frac{m - \alpha}{\frac{1}{K} + M_\infty} \quad (1.5)$$

where K is a constant and α is function of the $\frac{L}{D}$ ratio.

This formula is similar to the (1.4) found via analytical method, and the two are the same if $m_a + m_v = m$, $\gamma_v = \alpha$, $k_v = K$ and $a_c = a_\infty$.

The latter is the weakest hypothesis, since it's true only for low Mach numbers.

Heller[4, 5] corrected it by taking into account the increase in cavity temperature due to compression work and considering the speed of sound inside the cavity equal to the stagnation speed of sound:

$$f_m = \frac{U_\infty}{L} \cdot \frac{m - \alpha}{\frac{1}{k_v} + \frac{M_\infty}{\sqrt{1 + \frac{\gamma-1}{2} M_\infty^2}}} \quad (1.6)$$

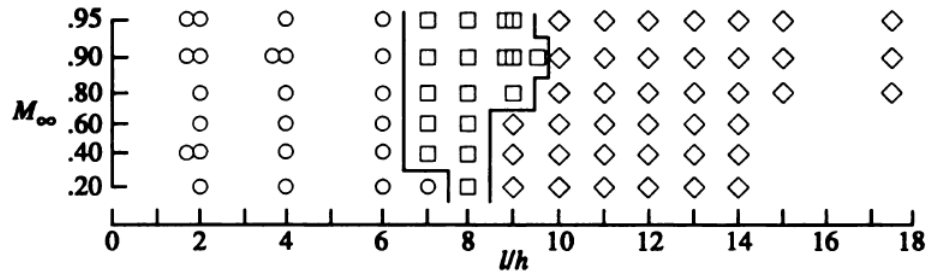
Furthermore, Rossiter found that

$$\begin{cases} \alpha = 0.062 \cdot \frac{L}{D} \\ k_v = 0.57 \end{cases} \quad (1.7)$$

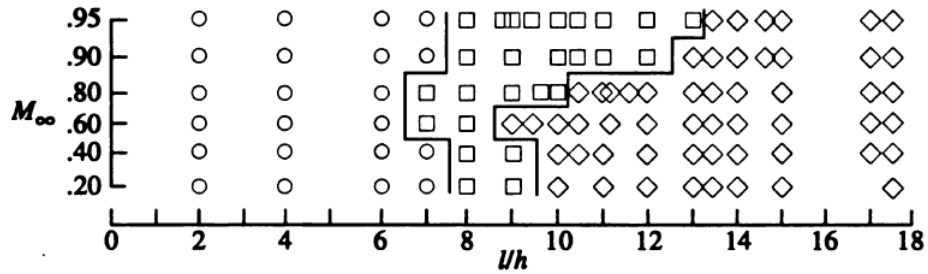
Subsequently, at the end of the 1990s[12], it was observed that in addition to open and closed cavity flows, the reattachment of the flow on the bottom of the cavity may not be stable, i.e. is intermittent. In this case, since the feedback mechanism is also intermittent, the periodic components of the fluctuations are strongly reduced, but not as negligible as when the reattachment is stable. The cavities where the flow behaves this way are known as *transitional cavity flows*. Maureen *et al.*[12] identified the threshold for having a closed cavity flow regime at length-to-depth ratios varying approximately between 8 and 14, being higher for larger width-to-depth ratios. His results are given in Figure 1.3.

The utilization of Computational Fluid Dynamics (CFD) techniques has enabled a deeper examination of the phenomenon. However, due to the substantial computational expense associated with simulations at high Reynolds numbers, the simulation of cavities in the transonic and supersonic regimes remains a challenging task[10]. It has been observed that Unsteady RANS (URANS) methods are able to predict the Rossiter modes, but they are by nature not able to predict the full spectrum of turbulent scales and, therefore, broadband components of pressure oscillations. In contrast, Detached Eddy Simulation (DES) and Large Eddy Simulation (LES) are able to predict both tonal and broadband components, and have proven to be more accurate. Some mixed RANS-LES techniques also seem to agree well with the experimental results[9, 10, 13].

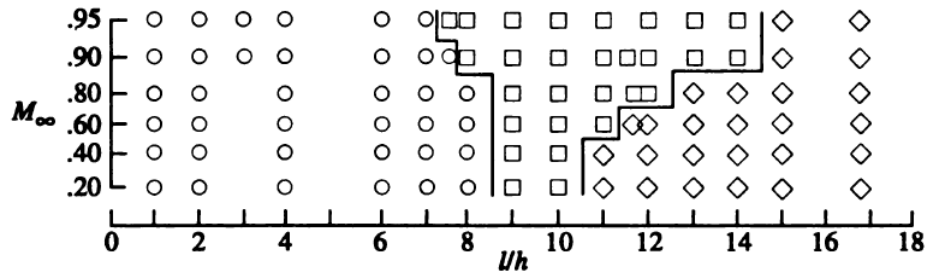
Some recent studies, however, have used the commercial software SIMULIA PowerFLOW[®] by *Dassault Systèmes* based on a Very Large Eddy Simulation (VLES) Lattice-Boltzmann Method (LBM)[1, 10]. The first of these works[10], led by Mancini *et al.*, analysed two cavities, one deeper and the other shallower, both in the high-subsonic and supersonic cases. They proposed a further correction to the Rossiter-Heller formula (eq. 1.6) in order to consider the reduction of the sound propagation time from the rear wall to the front wall of the cavity. In this way, the actual speed of the acoustic waves travelling upstream is $a_c(1 + M_c)$, where M_c is the reversed-flow convection Mach number inside the cavity. If the original



(a) $\frac{W}{D} = 1$



(b) $\frac{W}{D} = 2$



(c) $\frac{W}{D} = 4$

Figure 1.3: Boundaries of cavity flow regimes obtained by Maureen *et al.*[12] at different width-to-depth ratios. Circles indicate an open flow regime; squares a transitional flow; diamonds a closed flow.

formula is updated, the equation becomes

$$f_m = \frac{U_\infty}{L} \cdot \frac{(m - \alpha)(1 + M_c)}{\frac{1+M_c}{k_v} + \frac{M_\infty}{\sqrt{1 + \frac{\gamma-1}{2}M_\infty^2}}} \quad (1.8)$$

If $M_c = 0$, the two formulae are equal.

This correction ensures that the Rossiter modes frequencies obtained from the semi-empirical formula are much closer both to those obtained from wind tunnel measurements and to those obtained from the LBM simulation. The same study also proved that the reverse-flow Mach number in cavity depends both from free-stream Mach number and length-to-depth ratio, although it did not manage to demonstrate the dependence, being M_c higher in supersonic case for shallow cavities and vice versa for deep cavities, and used an average value of 0.18. Furthermore, it confirmed that Rossiter modes are predominantly longitudinal, with slightly spanwise variations, despite side edge vortices. Anyway, the paper proved that Rossiter modes frequencies and wall pressure oscillations can be properly described by the software for all cases.

A subsequent paper by the same authors[1] focused on expressing M_c as a function of the free-stream Mach number and cavity length-to-depth ratio. By relating M_c to the free-stream Mach number and the stagnation temperature in the cavity they obtained:

$$M_c = \frac{M_\infty}{\sqrt{1 + \frac{\gamma-1}{2}M_\infty^2}} \cdot \tilde{V}_c \quad (1.9)$$

where \tilde{V}_c is a function of $\frac{L}{D}$ and M_∞ and is derived via polynomial regression:

$$\tilde{V}_c = c_0 + c_1 \frac{L}{D} + c_2 M_\infty + c_3 \left(\frac{L}{D}\right)^2 + c_4 M_\infty^2 + c_5 M_\infty \frac{L}{D} \quad (1.10)$$

Two different sets of coefficients were used (relative to two different distances from the cavity floor) and the one with the less error compared to reference experimental data were chosen.

The same paper, also, improved the α function of cavity aspect ratio by replacing the linear fit made by Rossiter (eq. 1.7) with a second-order fit. The two corrections made led to an improvement in Rossiter modes prediction accuracy.

Due to the importance of the application of this phenomenon, several researches have been carried out to investigate possible control techniques, both active and passive.

Passive control consists of modifying the cavity, such as adding spoilers to the leading edge[11]. This causes the boundary layer to be deflected from the cavity and the shear layer to develop outside it, not impinging on the rear wall, thus avoiding

the feedback mechanism. However, the ramp angle must be properly calculated based on the cavity geometry and the flow velocity, making this modification ineffective in off-design conditions[3].

Active control techniques, instead, include injecting fluid from the front wall into the shear layer, along the whole span: this reduces the turbulent intensity and the size of the recirculation zone, reducing the positive feedback[3].

1.3 Aim of this Work

In this thesis a case of study with the above mentioned PowerFLOW software will be examined and analysed.

In Chapter 2 Boltzmann equation and the assumption underlying Lattice-Boltzmann Method will be presented, explaining how the macroscopic quantities are connected to the distribution function and how the common Navier-Stokes equations can be obtained from the Boltzmann one. The computational algorithm and how boundary conditions are implemented will be shown, and the above-mentioned software will then be briefly presented, explaining its steps.

In Chapter 3 the reference geometry will be presented and the preparation of the case to be simulated will be described step by step. The simulations performed will then be indicated and the results analysed: initially the temporal evolution of the flow in terms of boundary layer and vorticity will be shown, to then describe its mean field and turbulent kinetic energy. A comparison will then be made between three planes at different span positions to verify if, as stated in this Chapter, the phenomenon is predominantly longitudinal. Finally, the pressure oscillations will be analysed as Overall Sound Pressure Level and Sound Pressure Level, comparing the data obtained from the simulation with the experimental ones and with other numerical data present in the literature.

Chapter 2

The Lattice-Boltzmann Method and the PowerFLOW Software

The Lattice-Boltzmann Method (LBM) is a CFD technique that, unlike common methods based on the modelling of the Navier-Stokes equations, consists in the discretization of the Boltzmann equation, whose main variable is the probability density function $f(\vec{x}, \vec{\xi}, t)$ of a particle, described by its position \vec{x} and velocity $\vec{\xi}$ at a given time t . At the end of this Chapter, however, it is shown how from the Boltzmann equation the Navier-Stokes can be derived.

The basic idea of the method is that macroscopic fluid dynamics is nothing but the sum of the individual microscopic dynamics of the particles constituting it. However, since the number of fluid particles is so high that they can be modelled individually, they are described with a statistical approach through their distribution function[2].

The macroscopic physical quantities describing the fluid are connected to the moments of the function f . Indeed, the density ρ , the momentum density $\rho\vec{u}$ and the total energy ρE are, respectively, the zeroth, first and second moment of f with respect to $\vec{\xi}$ [18]:

$$\rho(\vec{x}, t) = \iiint f(\vec{x}, \vec{\xi}, t) d\vec{\xi} \quad (2.1a)$$

$$\rho(\vec{x}, t)\vec{u}(\vec{x}, t) = \iiint f(\vec{x}, \vec{\xi}, t)\vec{\xi} d\vec{\xi} \quad (2.1b)$$

$$\rho(\vec{x}, t)E(\vec{x}, t) = \frac{1}{2} \iiint f(\vec{x}, \vec{\xi}, t)(\vec{\xi} \cdot \vec{\xi}) d\vec{\xi} \quad (2.1c)$$

The other physical quantities are calculated from these.

The velocity $\vec{\xi}$ is the sum of the macroscopic velocity of the fluid \vec{u} and the microscopic velocity $\vec{\zeta}$, also called *peculiar velocity*. It is easy to prove that:

$$\iiint f\vec{\zeta} d\vec{\xi} = \iiint f\vec{\xi} d\vec{\xi} - \iiint f\vec{u} d\vec{\xi} = 0 \quad (2.2)$$

By making $\vec{\xi}$ explicit in (2.1c) we obtain:

$$\begin{aligned}
 \rho(\vec{x}, t)E(\vec{x}, t) &= \frac{1}{2} \iiint f(\vec{x}, \vec{\xi}, t)(\vec{\xi} \cdot \vec{\xi})d\vec{\xi} = \\
 &= \frac{1}{2} \iiint f(\vec{x}, \vec{\xi}, t)(\vec{u} + \vec{\zeta}) \cdot (\vec{u} + \vec{\zeta})d\vec{\xi} = \\
 &= \frac{1}{2} \iiint f(\vec{x}, \vec{\xi}, t)(\|\vec{u}\|^2 + \|\vec{\zeta}\|^2 + \vec{u} \cdot \vec{\zeta})d\vec{\xi} = \tag{2.3} \\
 &= \frac{1}{2} \iiint f(\vec{x}, \vec{\xi}, t)\|\vec{u}\|^2d\vec{\xi} + \frac{1}{2} \iiint f(\vec{x}, \vec{\xi}, t)\|\vec{\zeta}\|^2d\vec{\xi} = \\
 &= \frac{1}{2}\rho\|\vec{u}\|^2 + \frac{1}{2} \iiint f(\vec{x}, \vec{\xi}, t)\|\vec{\zeta}\|^2d\vec{\xi}
 \end{aligned}$$

Remembering that the total energy ρE is the sum of the kinetic energy $\frac{1}{2}\rho\|\vec{u}\|^2$ and the internal energy ρe , we get that the internal energy ρe is equal to:

$$\rho(\vec{x}, t)e(\vec{x}, t) = \frac{1}{2} \iiint f(\vec{x}, \vec{\xi}, t)(\vec{\zeta} \cdot \vec{\zeta})d\vec{\xi} \tag{2.4}$$

Pressure can, instead, be obtained by considering the variation in time of the momentum of particles on a surface, and considering that the effect in the three directions of motion is the same[17]. Hence, we obtain:

$$p(\vec{x}, t) = \frac{1}{3} \iiint \|\vec{\zeta}\|^2 f(\vec{x}, \vec{\xi}, t)d\vec{\xi} = \frac{2}{3}\rho(\vec{x}, t)e(\vec{x}, t) \tag{2.5}$$

From this relationship we obtain that the pressure is directly proportional to the internal energy: this is not at all unexpected considering that the greater the internal energy, the faster the individual particles move, therefore they impact more often and with more intensity on a surface.

This equation can also be compared with the ideal gas law:

$$p = \rho RT \tag{2.6}$$

where R is the specific gas constant, and is equal to $R = \frac{R_0}{\mathcal{M}}$, with $R_0 = 8.31 \frac{\text{J}}{\text{mol}\cdot\text{K}}$ the universal gas constant and \mathcal{M} the fluid molar mass.

R_0 can also be seen as the product of the Boltzmann constant $k_b = 1.38 \times 10^{-23} \text{ J/K}$ and the Avogadro number $N_A = 6.02 \times 10^{23} \text{ mol}^{-1}$, therefore:

$$p = \rho RT = \rho \frac{k_b N_A T}{\mathcal{M}} \tag{2.7}$$

Finally, since \mathcal{M} denotes the mass of a mole of particles, and N_A the number of particles in a mole, their ratio is equal to the mass m of a single particle:

$$p = \rho RT = \rho \frac{k_b T}{m} \tag{2.8}$$

Comparing the two, we obtain that:

$$e = \frac{3 k_b T}{2 m} \quad (2.9)$$

This will lately be used to calculate the equilibrium distribution.

2.1 The Boltzmann Equation

The Boltzmann equation states that the evolution of the distribution function $\frac{df}{dt}$ depends on collisions between particles, described by a *collision operator* Ω :

$$\frac{df}{dt} = \Omega \quad (2.10)$$

Collisions are certainly influenced by the positions and velocities of the particles just before they occur, so $\Omega = \Omega(f)$. Furthermore, $f = f(\vec{x}, \vec{\xi}, t)$, so:

$$\frac{df}{dt} = \frac{\partial f}{\partial \vec{x}} \frac{d\vec{x}}{dt} + \frac{\partial f}{\partial \vec{\xi}} \frac{d\vec{\xi}}{dt} + \frac{\partial f}{\partial t} = \Omega(f) \quad (2.11)$$

Considering that $\frac{d\vec{x}}{dt} = \vec{\xi}$ and that $\frac{d\vec{\xi}}{dt} = \frac{\vec{F}}{\rho}$, with \vec{F} indicating the external forces acting on the fluid, we obtain the *Boltzmann equation*:

$$\frac{df}{dt} = \frac{\partial f}{\partial t} + \vec{\xi} \frac{\partial f}{\partial \vec{x}} + \frac{\vec{F}}{\rho} \frac{\partial f}{\partial \vec{\xi}} = \Omega(f) \quad (2.12)$$

Collision Operator

The collision operator described by Boltzmann is the following[7]:

$$\Omega(f) = \int_{-\infty}^{+\infty} \int_0^{4\pi} n^2 (f^* f_1^* - f f_1) c \sigma d\Omega dc_1 \quad (2.13)$$

It models in detail the collision of each pair of particles, leading to a complex integral-differential equation. Since, as mentioned, the method is based on an average behaviour, it is possible to replace this operator with a simpler one, as identified by Bathgnar, Gross and Krook, called *BGK operator*[2]:

$$\Omega(f) = -\frac{1}{\tau} (f - f^{eq}) \quad (2.14)$$

The collision operator Ω is, in this way, related to the equilibrium distribution f^{eq} , since after the collision, the particles tend to return to the equilibrium state

CHAPTER 2. THE LATTICE-BOLTZMANN METHOD AND THE
POWERFLOW SOFTWARE

within a certain relaxation time τ . In theory, since this operator only considers binary collisions, its applicability would be limited to fluids where the diameters of the particles are much smaller than the distance between them, i.e. for dilute gases. However, its influence is very small, so the BGK operator can be safely used also for continuum flows[7]. Therefore, the equation (2.12) can be rewritten as:

$$\frac{\partial f}{\partial t} + \vec{\xi} \frac{\partial f}{\partial \vec{x}} + \frac{\vec{F}}{\rho} \frac{\partial f}{\partial \vec{\xi}} = -\frac{1}{\tau}(f - f^{eq}) \quad (2.15)$$

Furthermore, the collision operator must obey conservation laws for mass, momentum and energy[17], meaning:

$$\iiint \Omega(f) d\vec{\xi} = \iiint (f^{eq} - f) d\vec{\xi} = 0 \quad (2.16a)$$

$$\iiint \vec{\xi} \Omega(f) d\vec{\xi} = \iiint \vec{\xi} (f^{eq} - f) d\vec{\xi} = 0 \quad (2.16b)$$

$$\iiint (\vec{\xi} \cdot \vec{\xi}) \Omega(f) d\vec{\xi} = \iiint (\vec{\xi} \cdot \vec{\xi}) (f^{eq} - f) d\vec{\xi} = 0 \quad (2.16c)$$

$$\iiint (\vec{\zeta} \cdot \vec{\zeta}) \Omega(f) d\vec{\xi} = \iiint (\vec{\zeta} \cdot \vec{\zeta}) (f^{eq} - f) d\vec{\xi} = 0 \quad (2.16d)$$

Thus, substituting the equations (2.1), it is obtained that:

$$\iiint f^{eq}(\vec{x}, \vec{\xi}, t) d\vec{\xi} = \rho(\vec{x}, t) \quad (2.17a)$$

$$\iiint f^{eq}(\vec{x}, \vec{\xi}, t) \vec{\xi} d\vec{\xi} = \rho(\vec{x}, t) \vec{u}(\vec{x}, t) \quad (2.17b)$$

$$\frac{1}{2} \iiint f^{eq}(\vec{x}, \vec{\xi}, t) (\vec{\xi} \cdot \vec{\xi}) d\vec{\xi} = \rho(\vec{x}, t) E(\vec{x}, t) \quad (2.17c)$$

$$\frac{1}{2} \iiint f^{eq}(\vec{x}, \vec{\xi}, t) (\vec{\zeta} \cdot \vec{\zeta}) d\vec{\xi} = \rho(\vec{x}, t) e(\vec{x}, t) \quad (2.17d)$$

Moreover, from equations (2.17b) and (2.2) derives that:

$$\iiint f^{eq}(\vec{x}, \vec{\xi}, t) \vec{\zeta} d\vec{\xi} = 0 \quad (2.18)$$

Equilibrium Distribution

It is possible to assume that after a collision, particles' velocities are distributed in all directions around the mean velocity \vec{u} , meaning that the distribution function is dependant on the peculiar velocity[17]. Moreover, since the equilibrium distribution is independent of the direction, it is possible to separate the function f in different $\vec{\zeta}$ coordinates:

$$f^{eq}(\vec{\zeta}) = f_x^{eq}(\zeta_x) f_y^{eq}(\zeta_y) f_z^{eq}(\zeta_z) \quad (2.19)$$

This relationship is satisfied by Gaussian functions, i.e.:

$$f^{eq}(\vec{\zeta}) = a e^{-b \|\vec{\zeta}\|^2} \quad (2.20)$$

where a and b are two constants.

By substituting this expression of f^{eq} in equations (2.17a) and (2.17d):

$$\begin{cases} a = \rho \left(\frac{b}{\pi}\right)^{\frac{3}{2}} \\ b = \frac{3}{4e} \end{cases} \quad (2.21)$$

Substituting the (2.9), we obtain the *Maxwell-Boltzmann equilibrium distribution*:

$$f^{eq}(\vec{x}, \vec{\xi}, t) = \rho \left(\frac{m}{2\pi k_b T}\right)^{\frac{3}{2}} \cdot e^{-\frac{m \|\vec{\xi}\|^2}{2k_b T}} \quad (2.22)$$

More in general, if D is the number of dimensions of the problem (1, 2 or 3), the equilibrium distribution can be expressed as[19]:

$$f^{eq}(\vec{x}, \vec{\xi}, t) = \rho \left(\frac{m}{2\pi k_b T}\right)^{\frac{D}{2}} \cdot e^{-\frac{m \|\vec{\xi}\|^2}{2k_b T}} \quad (2.23)$$

2.2 The Lattice-Boltzmann Equation

The Lattice-Boltzmann Method consists of dividing the flow domain into a discrete lattice, applying two simplifications.

The first one is that external forces are negligible compared to the forces operating inside the collisions[7], while the second one is that particles can only occupy a finite number of positions in the grid; this leads to a discrete number of velocity directions. The different possible models are indicated by the notation **DkQb**, where k stands for the dimension of the space and b for the number of the velocity unitary vectors \vec{e}_i [7].

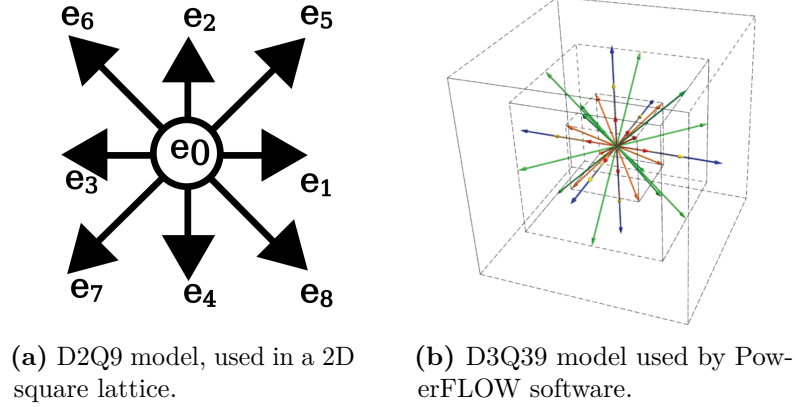


Figure 2.1: Two different velocity models, one two-dimensional and one three-dimensional.

E.g., in a two-dimensional square grid, a D2Q9 modes can be used, meaning particles are limited to nine possible velocities (Figure 2.1a).

Hence, the the equation (2.15) becomes:

$$\frac{\partial f_i}{\partial t} + \vec{\xi}_i \frac{\partial f_i}{\partial \vec{x}} = -\frac{1}{\tau}(f_i - f_i^{eq}) \quad \text{for } i = 0 \dots b \quad (2.24)$$

The microscopic velocity $\vec{\xi}_i$ in the direction \vec{e}_i can be expressed as $\vec{\xi}_i = c\vec{e}_i$. The magnitude c is called *lattice velocity*.

Integrating over a time interval Δt and a space interval Δx the function f :

$$\frac{f_i(\vec{x}, t + \Delta t) - f_i(\vec{x}, t)}{\Delta t} + c \frac{f_i(\vec{x} + \Delta \vec{x}, t + \Delta t) - f_i(\vec{x}, t + \Delta t)}{\Delta x} = -\frac{1}{\tau}(f_i - f_i^{eq}) \quad (2.25)$$

The lattice velocity c can be expressed ad $c = \frac{\Delta x}{\Delta t}$. An unitary lattice velocity is assumed, so that $\Delta \vec{x} = \vec{e}_i \Delta t$. Substituting this in the previous equation, the *Lattice-Boltzmann Equation* is obtained:

$$f_i(\vec{x} + \vec{e}_i \Delta t, t + \Delta t) - f_i(\vec{x}, t) = -\frac{\Delta t}{\tau}(f_i - f_i^{eq}) \quad (2.26)$$

where the quantity $\omega = \frac{\Delta t}{\tau}$ is called *collision frequency*.

Having a discrete number of velocities, the macroscopic quantities described by the integrals in the equations (2.1a) and (2.1b), are actually calculated as simple algebraic sums:

$$\rho = \sum_{i=0}^b f_i \quad (2.27a)$$

$$\rho \vec{u} = \sum_{i=0}^b f_i \vec{e}_i \quad (2.27b)$$

Finally, the equation (2.22) can be simplified via a second-order series expansion with respect to the velocity \vec{u} [2]:

$$f_i^{eq} = \rho w_i \left(1 + A(\vec{e}_i \cdot \vec{u}) + B(\vec{e}_i \cdot \vec{u})^2 + C \|\vec{u}\|^2 \right) \quad (2.28)$$

where w_i is a weighting factor and A , B and C are lattice constants. These constants can be calculated using the equations (2.17a) and (2.17b), moving from integrals to summations as done above.

2.3 Computational Algorithm

Any software that implements the LBM must manage the computational algorithm and the boundary and initial conditions. The computational algorithm can be seen as sum of a *collision phase* and a *propagation phase*: at each timestep, the particles incoming collide, modifying their distribution function according to the Lattice-Boltzmann equation

$$f_i(\vec{x} + \vec{e}_i \Delta t, t + \Delta t) = f_i(\vec{x}, t) - \frac{\Delta t}{\tau} (f_i - f_i^{eq})$$

and then they propagate in neighbouring cells, triggering a new collision in the next timestep[18].

So, the computational loop (schematized in Figure 2.2) consist in the following steps per each lattice cell:

1. From the distribution f_i , the macroscopic quantities ρ and \vec{u} are calculated, according the equations (2.27).
2. From ρ and \vec{u} , the equilibrium distribution f^{eq} is obtained through the (2.28).
3. The distribution functions after the collision are computed according to the RHS of the above equation.
4. The distribution functions propagate towards neighbouring cells, completing the above equation.

Then the cycle stars again, until a stop condition is met. The order of executing collision and propagation is arbitrary[18], meaning that either particles first propagate to adjacent cells and then particles in the same cell collide, and then they propagate again, or that particles in the same cell collide first and then they propagate to adjacent cells, and then they collide again.

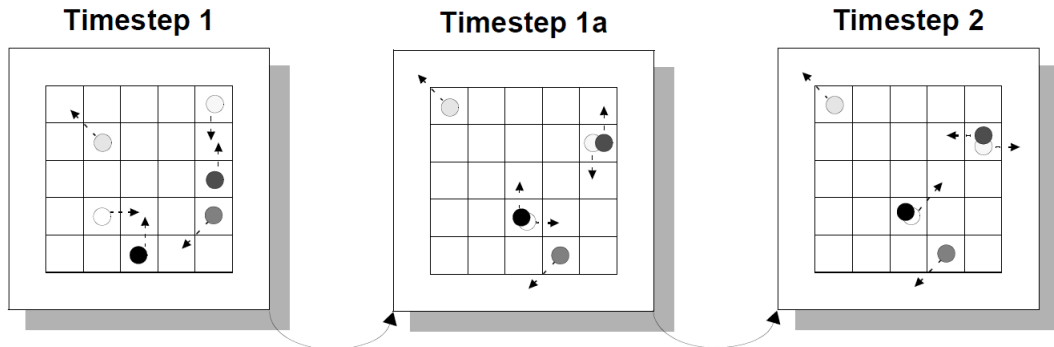


Figure 2.2: Schematization of the algorithm steps: here there is first the propagation step and the collision one.[14]

The first three steps are completely local, since only local quantities in each cell are used, while in the propagation step particles only propagate in neighbouring cells: hence, the Lattice-Boltzmann Method is suited for a large parallelization of the algorithm[17].

This cycle is preceded by an initialization, where for each cell initial conditions necessary to start the computational loop are applied.

Boundary Conditions

The boundary conditions are given as a function of the macroscopic quantities, therefore they must be transformed in order to be used in the LBM[18]. There are essentially three types of boundary conditions: *periodic*, *bounce back* and *Zou-He*[17].

Periodic conditions The simplest boundary conditions are periodic ones, where each cell is considered "adjacent" to those at the opposite corner of the domain: in this way the particles propagate from one corner to the opposite one, as in Figure 2.3a

Bounce back conditions Bounce back conditions are used to model no-slip conditions on a wall: cells are created so that the wall is "immersed" in the lattice (and not coincident with the cell boundaries). Particles propagating towards the wall are actually bounced back after the propagation step, meaning they maintain their distribution function, but with inverted velocity, as in Figure 2.3b.

The bounce back can be decomposed into normal and tangential: the first ensures that there is no mass flow through the wall, blocking the fluid, the second that the no-slip condition is valid. It is possible that only the normal bounce back

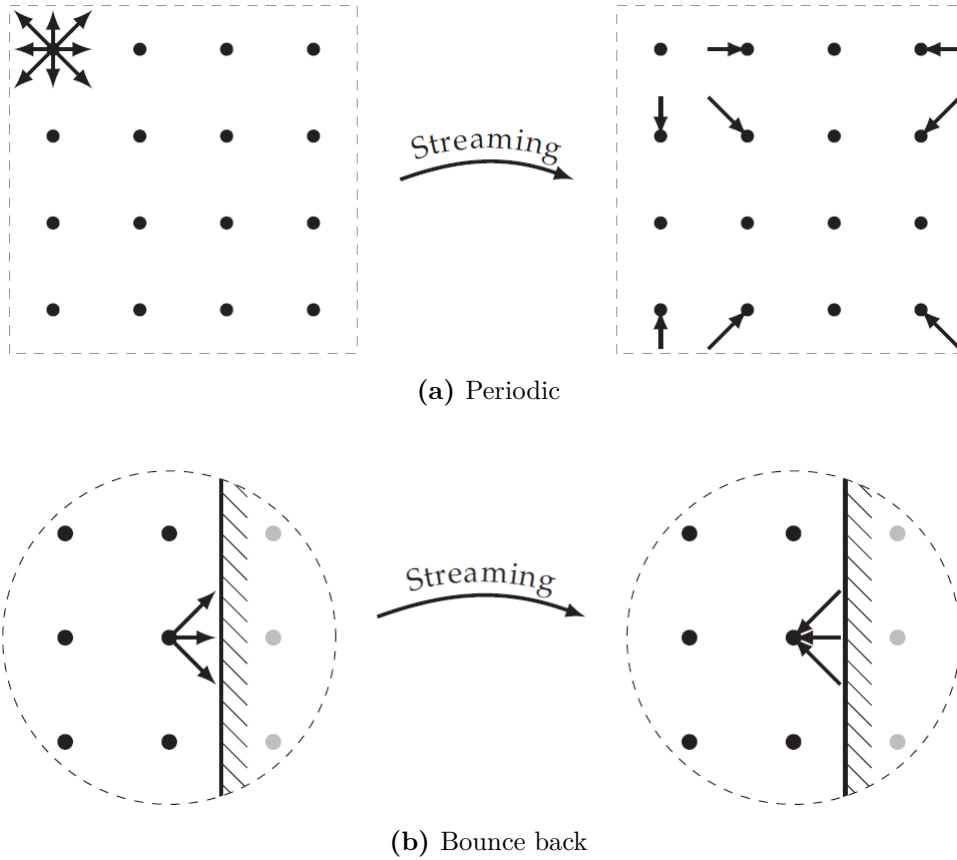


Figure 2.3: Example of boundary conditions in a D2Q9 model.[17]

is applied and not the tangential one, in this way the free-slip condition is modelled, as for a frictionless wall.

Zou-He conditions These are used to model a condition of a known physical quantity, such as an inlet or an outlet. In this case, after the propagation step, the distribution functions towards the boundary are maintained, while those moving away from it are calculated considering the equations (2.27), forcing the physical quantities to be those imposed by the boundary condition.

2.4 PowerFLOW Software

The PowerFLOW software implements this method. In a three-dimensional case, the lattice is made up of cubic volume elements, named *voxels*, and surface elements, called *surfels*, at the intersection between a solid body and a fluid are

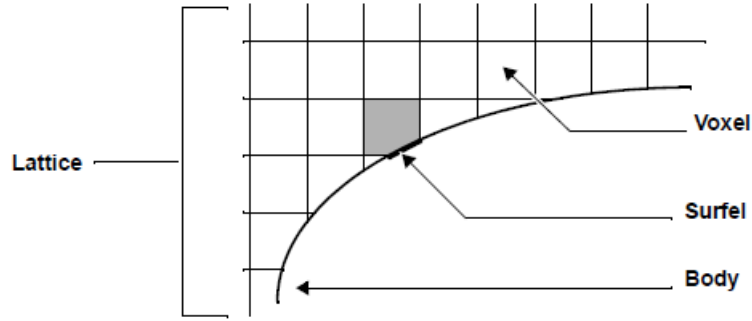


Figure 2.4: PowerFLOW lattice elements.[14]

1	2	2	2	2	2	2	1	
	2	2	2	2	2	2		
1	2	3	3	3	3	3	3	1
	2	3	3	3	3	3	2	
	2	3	3	3	3	3	2	
1	2	3	3	3	3	3	1	
	2	3	3	3	3	3		
1	2	2	2	2	2	2	1	
	2	2	2	2	2	2		
1	1	1	1	1	1	1	1	

Figure 2.5: Lattice refinement example with three different VR levels: the higher the level, the finer are the voxels.[18]

generated (Figure 2.4). A D3Q39 (which can be seen in Figure 2.1b) model is used[10].

Voxels have different sizes, according to their Variable Resolution (VR) level established during the creation of the case to be simulated. Moving from one VR level to the immediately lower one, voxels seize doubles (i.e. their volume increases by factor of 8), as in Figure 2.5, where moving from a VR level of 1 to a VR level of 2, the voxel size is halved.

Similarly, to ensure that the data is synchronized, as the voxel size doubles, the data update rate is halved, meaning that if the data in the densest region is updated every timestep, in the immediately less dense region, it is updated every two timesteps.

For high Reynolds numbers, a hybrid LBM/VLES approach is used[14]. Thus, a modified two-equations model $k-\varepsilon$ based on re-normalization group formulation[10] for turbulence is present, but it is not necessary to compute an eddy viscosity as in RANS. Instead, the turbulent kinetic energy k and the dissipation ε values

obtained from the two-equations system are used to calibrate the collision operator, modifying the relaxation time τ .

The PowerFLOW solver consists of 3 steps:

1. **Discretization:** the software automatically generates the grid for any geometry, according to the VR levels defined during case creation.
2. **Decomposition:** the case is prepared to be simulated in parallel on a multi-core system. Due to the intrinsic local nature of the method, it is efficiently run on clusters or multiple processors.
3. **Simulation:** the simulation itself is performed and the results are generated, acquiring data either from single points or from entire volumes.

2.5 Relation with Navier-Stokes Equations

At the end of this Chapter, we want to show how the Navier-Stokes equations, normally used in fluid dynamics and on which the most common numerical methods are based, can be derived from the Boltzmann equation.

First, the equation (2.15) is rewritten making the Cartesian components of the vectors explicit, indicating them with the Greek letters in subscript:

$$\frac{\partial f}{\partial t} + \sum_{\alpha} \xi_{\alpha} \frac{\partial f}{\partial x_{\alpha}} + \sum_{\alpha} \frac{F_{\alpha}}{\rho} \frac{\partial f}{\partial \xi_{\alpha}} = -\frac{1}{\tau} (f - f^{eq}) \quad (2.29)$$

Mass Conservation

The first equation, i.e. the conservation law for mass, can be obtained by integrating over $d\vec{\xi}$ the equation above:

$$\iiint \frac{\partial f}{\partial t} d\vec{\xi} + \iiint \sum_{\alpha} \xi_{\alpha} \frac{\partial f}{\partial x_{\alpha}} d\vec{\xi} + \iiint \sum_{\alpha} \frac{F_{\alpha}}{\rho} \frac{\partial f}{\partial \xi_{\alpha}} d\vec{\xi} = -\frac{1}{\tau} \iiint (f - f^{eq}) d\vec{\xi} \quad (2.30)$$

The RHS is null, from eq. (2.16a). Due to linearity, summations and integrals can be switched, while $\frac{F_{\alpha}}{\rho}$ is a constant and t and \vec{x} are not function of $\vec{\xi}$, so they can be take out from the integrals. Moreover, being $\vec{\xi}$ a merely coordinate in velocity space, it's independent of \vec{x} [17], so that $\xi_{\alpha} \frac{\partial f}{\partial x_{\alpha}} = \frac{\partial}{\partial x_{\alpha}} (\xi_{\alpha} f)$. This means:

$$\frac{\partial}{\partial t} \iiint f d\vec{\xi} + \sum_{\alpha} \frac{\partial}{\partial x_{\alpha}} \iiint \xi_{\alpha} f d\vec{\xi} + \sum_{\alpha} \frac{F_{\alpha}}{\rho} \iiint \frac{\partial f}{\partial \xi_{\alpha}} d\vec{\xi} = 0 \quad (2.31)$$

CHAPTER 2. THE LATTICE-BOLTZMANN METHOD AND THE
POWERFLOW SOFTWARE

The first and second integral are the density moment (2.1a) and the momentum moment (2.1b), while the third one can be valued through the Stokes theorem:

$$\iiint \frac{\partial f}{\partial \xi_\alpha} d\vec{\xi} = \iint_{\partial \vec{\xi}} f d\vec{\xi} \quad (2.32)$$

Since it's impossible for a particle to have infinite velocity, $f \rightarrow 0$ when $\vec{\xi} \rightarrow \infty$, so the surface integral is null. Therefore, the above equation becomes:

$$\frac{\partial}{\partial t} \rho + \sum_{\alpha} \frac{\partial}{\partial x_{\alpha}} (\rho u_{\alpha}) = 0 \quad (2.33)$$

which can be re-written as:

$$\frac{\partial \rho}{\partial t} + \nabla \cdot (\rho \vec{u}) = 0 \quad (2.34)$$

which is exactly the continuity equation.

Momentum Conservation

Momentum conservation equation can be obtained multiplying the equation (2.29) by ξ_{α} and integrating over $d\vec{\xi}$:

$$\iiint \xi_{\alpha} \frac{\partial f}{\partial t} d\vec{\xi} + \iiint \xi_{\alpha} \sum_{\beta} \xi_{\beta} \frac{\partial f}{\partial x_{\beta}} d\vec{\xi} + \iiint \xi_{\alpha} \sum_{\beta} \frac{F_{\beta}}{\rho} \frac{\partial f}{\partial \xi_{\beta}} d\vec{\xi} = -\frac{1}{\tau} \iiint \xi_{\alpha} (f - f^{eq}) d\vec{\xi} \quad (2.35)$$

By the same considerations made before, the equation becomes:

$$\frac{\partial}{\partial t} \iiint \xi_{\alpha} f d\vec{\xi} + \sum_{\beta} \frac{\partial}{\partial x_{\beta}} \iiint \xi_{\alpha} \xi_{\beta} f d\vec{\xi} + \sum_{\beta} \frac{F_{\beta}}{\rho} \iiint \xi_{\alpha} \frac{\partial f}{\partial \xi_{\beta}} d\vec{\xi} = -\frac{1}{\tau} \iiint \xi_{\alpha} (f - f^{eq}) d\vec{\xi} \quad (2.36)$$

From eq. (2.17b), the RHS is null, while from eq. (2.1b) the first integral is equal to ρu_{α} . The third integral can be obtained integrating by parts:

$$\iiint \xi_{\alpha} \frac{\partial f}{\partial \xi_{\beta}} d\vec{\xi} = - \iiint \frac{\partial \xi_{\alpha}}{\partial \xi_{\beta}} f d\vec{\xi} \quad (2.37)$$

It is clear that $\frac{\partial \xi_{\alpha}}{\partial \xi_{\beta}} = 1$ if $\alpha = \beta$ and 0 otherwise, so:

$$\begin{aligned} \iiint \xi_{\alpha} \frac{\partial f}{\partial \xi_{\beta}} d\vec{\xi} &= -\delta_{\alpha\beta} \iiint f d\vec{\xi} = -\rho \delta_{\alpha\beta} \Rightarrow \\ \Rightarrow \sum_{\beta} \frac{F_{\beta}}{\rho} \iiint \xi_{\alpha} \frac{\partial f}{\partial \xi_{\beta}} d\vec{\xi} &= -\sum_{\beta} F_{\beta} \delta_{\alpha\beta} = -F_{\alpha} \end{aligned} \quad (2.38)$$

where $\delta_{\alpha\beta}$ is the Kronecker delta.

The second integral, instead, can be calculated by considering that $\xi_\alpha \xi_\beta = (u_\alpha + \zeta_\alpha)(u_\beta + \zeta_\beta)$:

$$\begin{aligned} \iiint \xi_\alpha \xi_\beta f d\vec{\xi} &= \iiint (u_\alpha + \zeta_\alpha)(u_\beta + \zeta_\beta) f d\vec{\xi} = \\ &= \iiint u_\alpha u_\beta f d\vec{\xi} + \iiint u_\alpha \zeta_\beta f d\vec{\xi} + \iiint u_\beta \zeta_\alpha f d\vec{\xi} + \iiint \zeta_\alpha \zeta_\beta f d\vec{\xi} = \\ &= u_\alpha u_\beta \iiint f d\vec{\xi} + u_\alpha \iiint \zeta_\beta f d\vec{\xi} + u_\beta \iiint \zeta_\alpha f d\vec{\xi} + \iiint \zeta_\alpha \zeta_\beta f d\vec{\xi} \end{aligned} \quad (2.39)$$

The first term is equal to $\rho u_\alpha u_\beta$ and represents the macroscopic flow momentum, the second and third one are nulls from the (2.2), while the fourth term represents a diffusion of momentum[17]. If we define $\sigma_{\alpha\beta} = -\iiint \zeta_\alpha \zeta_\beta f d\vec{\xi}$, we obtain the momentum conservation equation:

$$\frac{\partial}{\partial t}(\rho u_\alpha) + \sum_\beta \frac{\partial}{\partial x_\beta}(\rho u_\alpha u_\beta - \sigma_{\alpha\beta}) - F_\alpha = 0 \quad (2.40)$$

which in vectorial form is:

$$\frac{\partial(\rho \vec{u})}{\partial t} + \nabla \cdot (\rho \vec{u} \vec{u}) = \nabla \cdot \hat{\sigma} + \vec{F} \quad (2.41)$$

where $\hat{\sigma}$ can be identified with the *Cauchy stress tensor*.

Energy Conservation

Finally, the last conservation equation can be obtained multiplying the equation (2.29) by $\frac{\xi_\alpha \xi_\alpha}{2}$ and integrating:

$$\frac{1}{2} \frac{\partial}{\partial t} \iiint \xi_\alpha \xi_\alpha f d\vec{\xi} + \frac{1}{2} \sum_\beta \frac{\partial}{\partial x_\beta} \iiint \xi_\alpha \xi_\alpha \xi_\beta f d\vec{\xi} + \frac{1}{2} \sum_\beta \frac{F_\alpha}{\rho} \iiint \xi_\alpha \xi_\alpha \frac{\partial f}{\partial \xi_\beta} d\vec{\xi} = 0 \quad (2.42)$$

Again, the RHS is null because of the (2.17c). The first integral is equal to ρE (eq. 2.1c), while the second and third ones can be calculated with a similar method as for the momentum equation:

$$\frac{1}{2} \sum_\beta \frac{F_\beta}{\rho} \iiint \xi_\alpha \xi_\alpha \frac{\partial f}{\partial \xi_\beta} d\vec{\xi} = - \sum_\alpha F_\alpha u_\alpha \quad (2.43a)$$

$$\frac{1}{2} \sum_\beta \frac{\partial}{\partial x_\beta} \iiint \xi_\alpha \xi_\alpha \xi_\beta f d\vec{\xi} = - \sum_\alpha \frac{\partial}{\partial x_\alpha} \left(\rho u_\alpha E - \sum_\beta (\sigma_{\alpha\beta} u_\beta) + \frac{1}{2} \iiint \zeta_\alpha \|\zeta\|^2 f d\vec{\xi} \right) \quad (2.43b)$$

Defining $q_\alpha = \frac{1}{2} \iiint \zeta_\alpha \|\zeta\|^2 f d\vec{\xi}$, the total energy conservation equation is obtained:

$$\frac{\partial}{\partial t}(\rho E) + \sum_\alpha \left[\frac{\partial}{\partial x_\alpha}(\rho E u_\alpha - \sum_\beta (\sigma_{\alpha\beta} u_\beta) + q_\alpha) - F_\alpha u_\alpha \right] = 0 \quad (2.44)$$

which can be re-written in a simpler way:

$$\frac{\partial(\rho E)}{\partial t} + \nabla \cdot (\rho E \vec{u}) = \nabla \cdot (\hat{\sigma} \cdot \vec{u}) + \vec{F} \cdot \vec{u} - \nabla \cdot \vec{q} \quad (2.45)$$

where \vec{q} is the *heat flux*.

Stress Tensor and Heat Flux

In the last two equations, $\hat{\sigma}$ and \vec{q} have been defined in relation to f . However, it can be shown that in reality they depend only on macroscopic quantities: the distribution function f is expanded around the equilibrium distribution $f^{(0)} = f^{eq}$ through a sum of perturbed functions $f^{(n)}$, such that $\frac{f^{(n)}}{f^{eq}} = \mathcal{O}(Kn^n)$, where Kn is the *Knudsen number*[17]:

$$f = f^{eq} + \varepsilon f^{(1)} + \mathcal{O}(Kn^2) \quad (2.46)$$

Similarly, $\hat{\sigma}$ and \vec{q} can be expanded too:

$$\hat{\sigma} = \hat{\sigma}^{(0)} + \varepsilon \hat{\sigma}^{(1)} + \mathcal{O}(Kn^2) \quad (2.47a)$$

$$\vec{q} = \vec{q}^{(0)} + \varepsilon \vec{q}^{(1)} + \mathcal{O}(Kn^2) \quad (2.47b)$$

with

$$\sigma_{\alpha\beta}^{(n)} = - \iiint \zeta_\alpha \zeta_\beta f^{(n)} d\vec{\xi} \quad \text{and} \quad q_\alpha^{(n)} = \frac{1}{2} \iiint \zeta_\alpha \|\zeta\|^2 f^{(n)} d\vec{\xi} \quad (2.48)$$

From equations (2.5) and (2.18) can be obtained $\hat{\sigma}^{(0)}$ and $\vec{q}^{(0)}$:

$$\sigma_{\alpha\beta}^{(0)} = -p\delta_{\alpha\beta} \quad (2.49a)$$

$$q_\alpha^{(0)} = 0 \quad (2.49b)$$

$\hat{\sigma}^{(1)}$ and $\vec{q}^{(1)}$ are, instead, obtained by substituting the (2.46) in the (2.15), dividing both sides by f^{eq} , and obtaining $f^{(1)}$ as a function of the latter. Then replacing f^{eq} with its expression as in (2.22) and calculating the integrals, we obtain that[17]:

$$\sigma_{\alpha\beta} = -p\delta_{\alpha\beta} + p\tau \left(\frac{\partial u_\alpha}{\partial x_\beta} + \frac{\partial u_\beta}{\partial x_\alpha} - \frac{2}{3}\delta_{\alpha\beta} \sum_\gamma \frac{\partial u_\gamma}{\partial x_\gamma} \right) \quad (2.50a)$$

$$q_\alpha = -\rho e\tau \frac{10}{9} \frac{\partial e}{\partial x_\alpha} \quad (2.50b)$$

CHAPTER 2. THE LATTICE-BOLTZMANN METHOD AND THE
POWERFLOW SOFTWARE

From Newtonian-Stokesian fluids constitutive relationship and from Fourier law, we know that:

$$\sigma_{\alpha\beta} = -p\delta_{\alpha\beta} + \mu \left(\frac{\partial u_\alpha}{\partial x_\beta} + \frac{\partial u_\beta}{\partial x_\alpha} - \frac{2}{3}\delta_{\alpha\beta} \sum_\gamma \frac{\partial u_\gamma}{\partial x_\gamma} \right) \quad (2.51a)$$

$$q_\alpha = \kappa \frac{\partial T}{\partial x_\alpha} \quad (2.51b)$$

Therefore, it is obtained that:

$$\begin{cases} \mu = p\tau \\ \kappa = \frac{5}{2}\rho R^2 T\tau \end{cases} \quad (2.52)$$

The transport coefficients μ and κ are, therefore, derived as a function of the relaxation time τ , instead of being empirical parameters of the fluid.

Substituting, therefore, the relations just obtained in the equations of conservation of momentum and energy, we obtain the common Navier-Stokes equations:

$$\frac{\partial \rho}{\partial t} + \nabla \cdot (\rho \vec{u}) = 0 \quad (2.53a)$$

$$\frac{\partial(\rho \vec{u})}{\partial t} + \nabla \cdot (\rho \vec{u} \vec{u}) = -\nabla p + \nabla \cdot \left(\mu (\nabla \vec{u} + \nabla \vec{u}^T - \frac{2}{3}(\nabla \cdot \vec{u}) \hat{\mathbf{I}}) \right) + \vec{F} \quad (2.53b)$$

$$\frac{\partial(\rho E)}{\partial t} + \nabla \cdot (\rho E \vec{u}) = -p \nabla \cdot \vec{u} + \nabla \cdot \left(\mu (\nabla \vec{u} + \nabla \vec{u}^T - \frac{2}{3}(\nabla \cdot \vec{u}) \hat{\mathbf{I}}) \cdot \vec{u} \right) + \vec{F} \cdot \vec{u} + \nabla \cdot (\kappa \nabla T) \quad (2.53c)$$

Chapter 3

A Case of Study: the M219 Cavity

In 2000, Henshaw[6] collected several experimental data relating to a particular geometry, called the M219 cavity. This cavity has been used as a benchmark for subsequent CFD techniques, including those mentioned in Chapter 1. The geometry is depicted in Figure 3.1: the cavity has two configurations: one deeper and one shallower.

On the cavity floor there are ten Kulite pressure transducers, whose position along the cavity is indicated in Table 3.1 on the following page. For the deeper case, Kulite probes are located on the rig centre line, which is displaced by 1 inch from the cavity centre line; while, for the shallower case, the probes are on the cavity centre line. Henshaw collected data for both configurations at three different Mach numbers (0.6, 0.85 and 1.35).

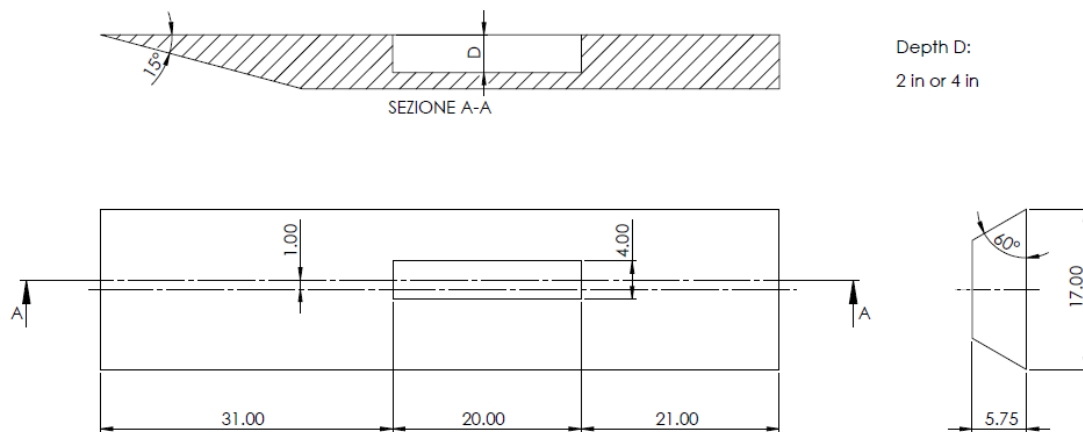


Figure 3.1: M219 Cavity. Dimensions are in inches.

Table 3.1: Kulite transducers position

Probe	x (in)	x/L
k20	1	0.05
k21	3	0.15
k22	5	0.25
k23	7	0.35
k24	9	0.45
k25	11	0.55
k26	13	0.65
k27	15	0.75
k28	17	0.85
k29	19	0.95

In this work, the deep cavity in the transonic case has been chosen to validate the LBM using the software PowerFLOW, meaning a cavity depth of 4 inches and a Mach number of 0.85.

3.1 Case Preparation

Geometry The chosen geometry has been recreated in a CAD environment, using the commercial software SolidWorks by *Dassault Systèmes* – the same company as PowerFLOW – and then imported into the PowerCASE software, used for preprocessing. A box has been then created around the test rig to simulate the wind tunnel, whose dimensions are shown in Figure 3.2. The coordinate system used can be seen in Figure 3.3 on the next page.

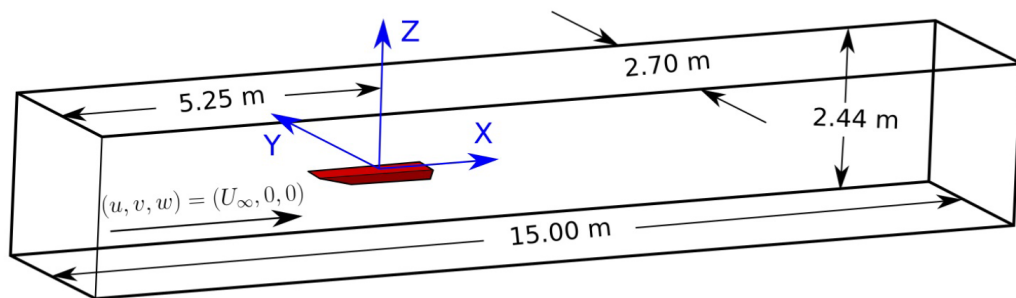


Figure 3.2: Wind tunnel dimensions.[13]

Ten probes have been added to the bottom of the cavity for data acquisition, positioned like the Kulite pressure transducers of the Henshaw experiment.

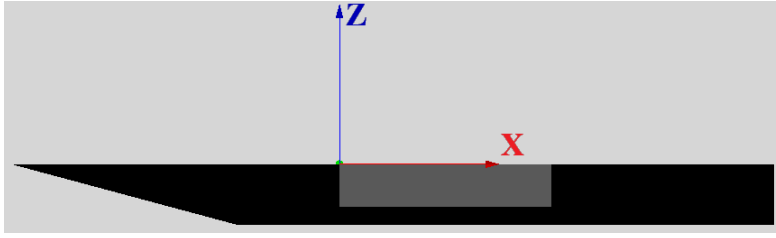


Figure 3.3: Coordinate System.

Table 3.2: Boundary conditions at inlet and outlet.

Total Pressure Inlet	
p_0 [Pa]	T_0 [K]
102 149	302
Pressure Outlet	
p [Pa]	
63 691	

Boundary and Initial Conditions Thereafter, the boundary conditions have been set: first boundaries have been created as thin boxes around the tunnel walls (see Figure 3.4b), and then the conditions have been implemented. The test rig surfaces have been assigned a standard wall condition, while the tunnel side walls, as well as the ceiling and floor, have been modelled as frictionless walls; the inlet as a total pressure inlet, setting p_0 and T_0 , and the outlet as a pressure outlet, setting a pressure calculated from p_0 and M .

Finally, the initial fluid conditions have been set, with standard γ , c_p and ν , and pressure, temperature and velocity calculated from p_0 , T_0 and the Mach number.

The boundary conditions are summarized in Table 3.2; the fluid initial conditions in Table 3.3.

Table 3.3: Fluid initial conditions.

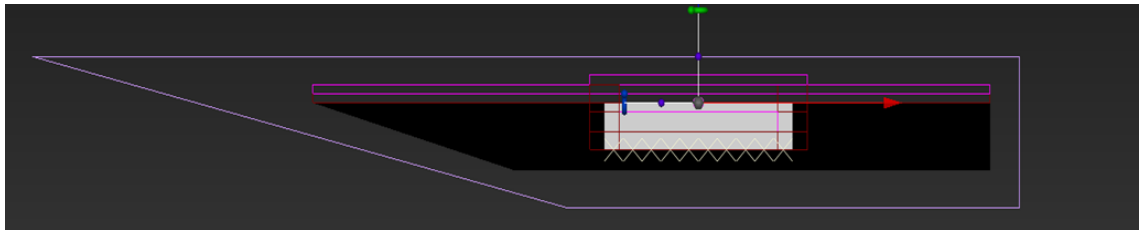
γ	1.4
c_p [J/(kgK)]	1005
ν [m ² /s]	1.5×10^{-5}
T [K]	263.87
p [Pa]	63 691
U_∞ [m/s]	277

VR Regions The next step is to define the refinement regions of the domain, as described in Chapter 2. The highest VR level, meaning the finest region, is assigned to the:

- test rig boundary layer;
- cavity boundary layer;
- cavity shear layer.

These are the red ones in Figure 3.4a. In the same picture, the magenta regions have the voxel size one time bigger, and is an offset of the red one; while in the purple region the voxel size is two times bigger, and is defined as a test rig offset.

The subsequent regions (Figure 3.4b) are constructed as increasingly larger boxes, until reaching the boundaries of the domain. The dimensions of each region are calculated to have a minimum of 10 voxels per region, thereby reducing the numerical errors that may arise at the interface between two regions due to the variation in voxel size.



(a) VR Regions near the test rig. The white *Xs* are the probes located as the Kulite transducers (Table 3.1).



(b) VR Regions stepping away from the test rig. Here it is also possible to notice the domain boundaries, created as thin boxes: the ceiling and floor of the gallery (in white), the inlet (in green) and the outlet (in red).

Figure 3.4: VR Regions in the flow domain.

Frequency Range Lastly, it is necessary to establish the frequency range within which the analyses are performed. Indeed, the dimensions of the voxels and the acquisition time depend on the extremes of the range.

Table 3.4: Frequency range of the simulation.

f_{min} [Hz]	f_{max} [Hz]
100	2500

The size of the voxels in the finest region derives from the maximum frequency: a sufficient number of voxels for each wavelength is necessary to best describe pressure oscillations, avoiding aliasing phenomena. Given c the velocity and f_{max} the maximum frequency, the size of the smallest voxels is equal to:

$$\text{smallest voxel size} = \frac{1}{N} \frac{c}{f_{max}} \quad (3.1)$$

where N is the number of desired voxels for each wavelength. Since we want to capture both pressure oscillations caused by vortices and those caused by sound, the velocity c must be the smallest between the speed of sound a_c and the speed of vortical structures, equal to $0.57 \cdot U_\infty$ (Chapter 1). Thus, the higher the maximum frequency, the smaller the voxels will be.

The minimum frequency, on the other hand, influences the data acquisition time, since it is necessary to simulate for enough periods for the mean flow to be stationary. The period T is equal to $\frac{1}{f_{min}}$, so the lower the minimum frequency, the longer the acquisition time.

The frequency range for this simulation is reported in Table 3.4.

Data Acquisition Data sampling happens at the ten probes on the cavity floor, as well as on three planes cutting the cavity, placed at one-quarter ($y = -1$ in), one-half ($y = 0$ in) and three-quarters ($y = 1$ in) of its spanwise dimension, with an acquisition frequency three times higher than the maximum frequency, according to Nyquist criterion.

3.2 Simulation

The simulations were performed with the PowerFLOW software on the *Legion* server of the Politecnico HPC, whose technical characteristics are reported in Figure 3.6.

A first simulation was performed with a coarse grid, with 30 voxels per wavelength in the finest region and an acquisition time of 40 periods. This means almost 5 million voxels and a saving time of nearly 0.4s, and the simulation took about 5 hours on 32 cores, i.e. 160 CPU hours. At the end of the simulation a checkpoint was generated, which was used as a seed to initialize the next simulation.

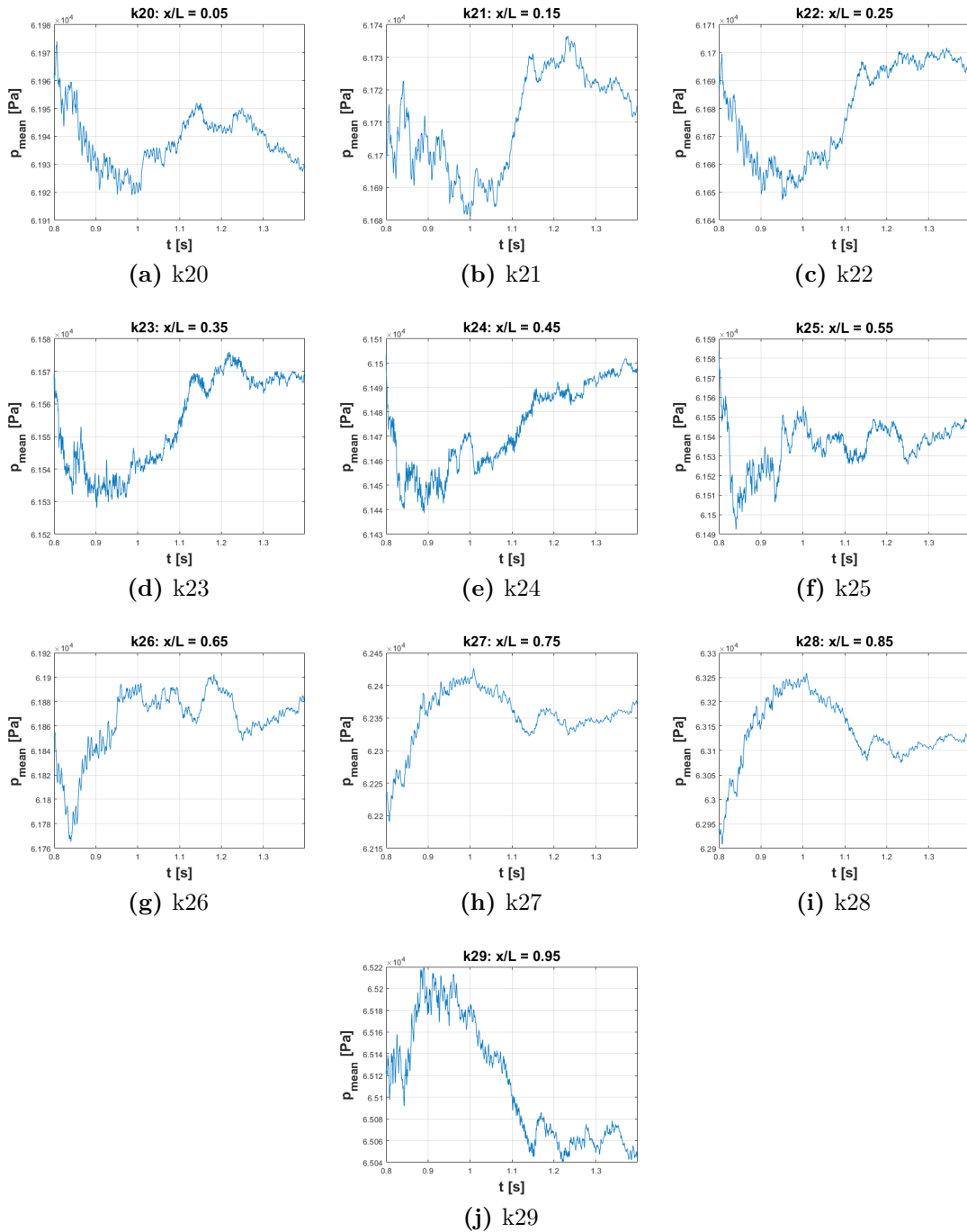


Figure 3.5: Mean pressure trend in time in the Kulite probes after the 2nd simulation.

Architecture	Linux Infiniband-EDR MIMD Distributed Shared-Memory Cluster
Node Interconnect	Infiniband EDR 100 Gb/s
Service Network	Gigabit Ethernet 1 Gb/s
CPU Model	2x Intel Xeon Scalable Processors Gold 6130 2.10 GHz 16 cores
GPU Model	4x nVidia Tesla V100 SXM2 - 32 GB - 5120 cuda cores (on 6 nodes)
Sustained performance (Rmax)	21.094 TFLOPS (last update: july 2019) [14 nodes]
Peak performance (Rpeak)	110.865 TFLOPS (last update: july 2020) [57 nodes]
Computing Cores	1824
Number of Nodes	57
Total RAM Memory	21.888 TB DDR4 REGISTERED ECC
OS	Centos 7.6 - OpenHPC 1.3.8.1
Scheduler	SLURM 18.08.8

Figure 3.6: HPC *Legion* server technical specifications.[20]

The second simulation was then launched with a finer grid and a longer acquisition time, considering twice the voxels per wavelength in the finest region and twice the saving time, for a total of about 32 million voxels and 52 h/1660 CPU hours.

At the end of this simulation, the trend of the mean probe pressure over time was plotted, in order to verify that the transient regime is concluded, meaning the average flow has reached steadiness. This is reported in Figure 3.5. As can be seen, the steadiness of the mean flow has not yet been reached: therefore, a further simulation with a longer time is necessary.

For the third simulation, the number of voxels per wavelength was doubled again, reaching a total of approximately 296 million. Once again, the checkpoint generated at the end of the previous simulation was used as a seed to initialize this simulation. Regrettably, this simulation could not have been completed.

The simulation times, as well as the number of voxels and their size in the region with the highest VR level, are summarized in Table 3.5.

Table 3.5: Voxel dimension and simulation time of the three simulation performed.

	Number of voxels	Smallest voxel size	CPU hours
Coarse grid	~5 million	2.1 mm	160
Medium grid	~32 million	1.3 mm	1660
Fine grid	~296 million	0.67 mm	/

3.3 Results Analysis

The results obtained have been analysed using the PowerVIZ and PowerACOUSTICS software. As seen in Chapter 1, the parameters that determine the nature of the cavity flow are the width-to-depth and length-to-depth ratios, and the Mach number. For a ratio $\frac{W}{D} = 1$ and a ratio $\frac{L}{D} = 5$, at a Mach number of 0.85, according to Figure 1.3a on page 6, an open cavity flow can be predicted.

Flow Evolution

The evolution of the flow in a mid-span plane can be observed in Figure 3.7, where the mean streamwise velocity field at different time instants is reported. The black line indicates the point where the x-velocity u is equal to $0.99 \cdot U_\infty$, which can be conventionally considered the border of the boundary layer. The point where the boundary layer rapidly decreases and then grows again is the reattachment point. As can be seen, the boundary layer on the test rig separates from the front edge of the cavity, and then reattaches on the rear edge, or even downstream of it. Therefore, we are in the case of open cavity flow, as we expected.

The red line, instead, is an iso-line at $u = 0$, identifying the region with negative x-velocity, i.e. an upstream flow: this is the recirculation region, where a reverse flow is formed from a high-pressure zone and a low-pressure one.

The flow behaviour can be observed through the streamlines, reported in Figure 3.8: far from the cavity the flow is undisturbed, while in proximity of the cavity it is deflected by the shear layer; it is also possible to note the streamline that impinges on the rear lip: this is at the basis of the feedback mechanism (responsible for the strong tonal components of pressure oscillation), because the acoustic waves generated in this way interact with the vortices of the shear layer.

Inside the cavity, and in particular starting from the rear wall, the recirculation bubble is formed, consisting of two clockwise vortices. A second vortex, smaller and counter-clockwise, is present near the front wall.

The streamlines are superimposed on the plot of the vorticity component $\omega_y = \frac{1}{2} \left(\frac{\partial u}{\partial z} - \frac{\partial w}{\partial x} \right)$, whose behaviour over time is reported in Figure 3.9. Observing the temporal evolution of vorticity, it can be seen that the vortices of the shear layer propagate downstream, while those in the cavity, due to the recirculation zone, move upstream and simultaneously upwards, following the recirculation bubble.

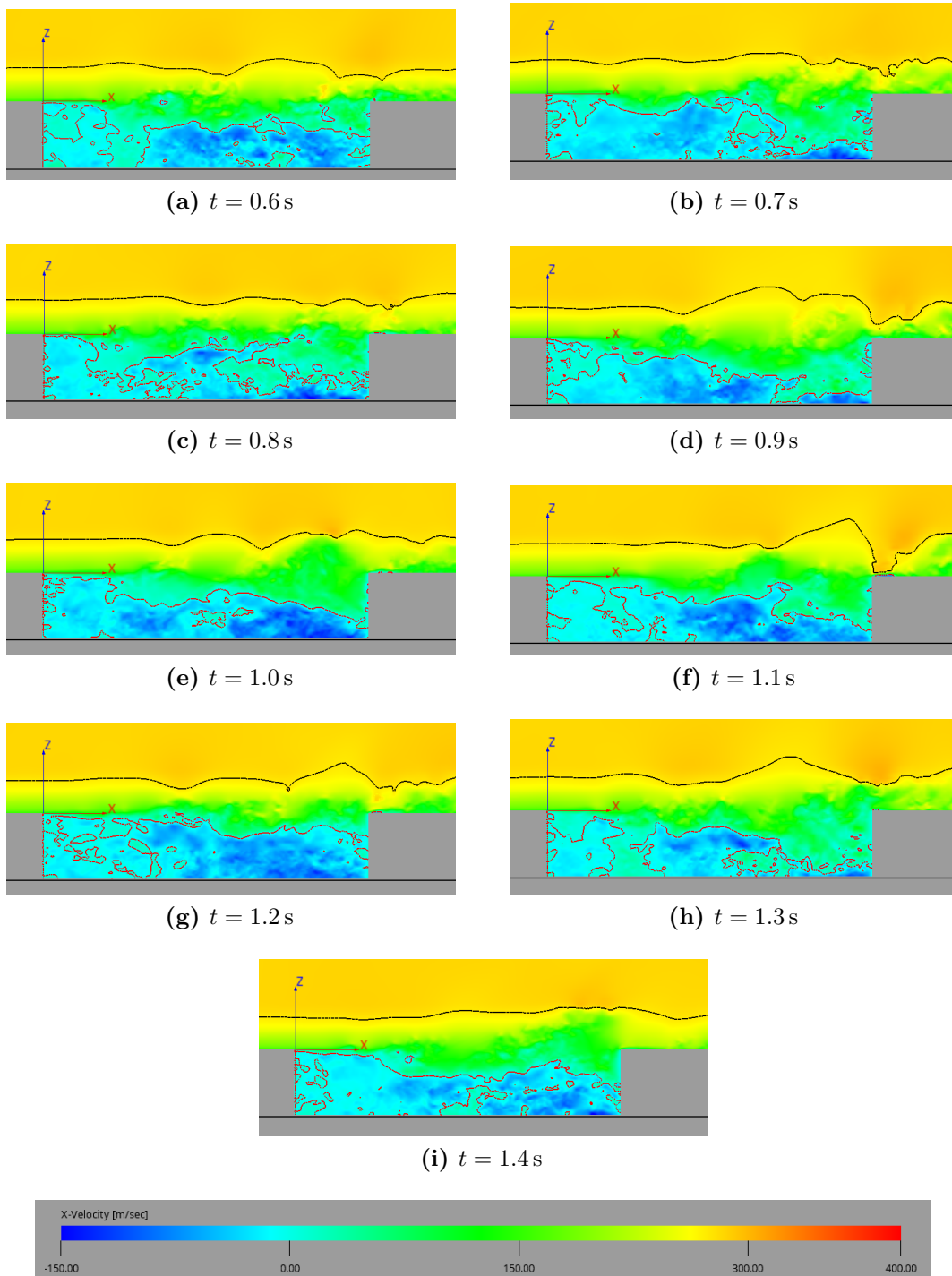


Figure 3.7: Streamwise velocity u evolution in a mid-span plane.

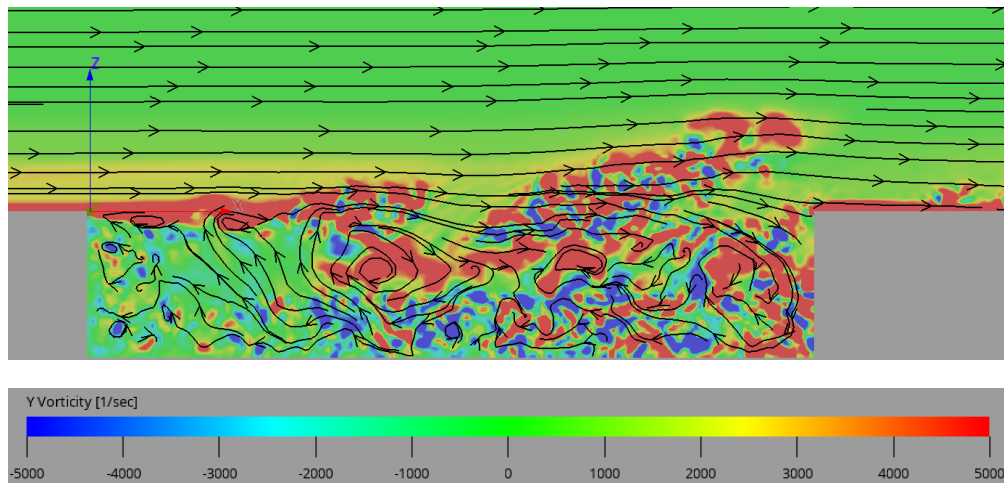


Figure 3.8: Streamlines in a mid-span plane, at $t = 1.4$ s, superimposed over the vorticity field ω_y .

Mean Field

Figure 3.10 reports the streamlines superimposed over the mean streamwise velocity field U . Above the cavity, the mean velocity is constant and slightly greater than the velocity U_∞ , since the test rig slightly reduces the tunnel section, accelerating the flow. An even greater increase would be observed if there were a boundary layer on the tunnel walls, which however in this simulation have been modelled as frictionless.

Then there is a constant mean velocity in the boundary layer on the rig, both upstream and downstream of the cavity, and in the shear layer. Inside the cavity, instead, there is a slightly negative or null mean velocity in the first half, while in the second half there are negative velocities with a high magnitude on the bottom and progressively greater velocities with the increase of z , until reaching positive velocities. This behaviour is consistent with the recirculation bubble identified by the streamlines: the flow has a positive streamwise velocity in the shear layer and a negative vertical velocity near the rear wall, so at the bottom of the cavity the streamwise velocity becomes negative and the vertical velocity positive, until it rejoins the shear layer.

This can be better seen looking at the mean velocity profiles, as in Figure 3.11. Near the front edge, the mean velocity in the cavity is almost null, while moving downstream zero mean velocity point shifts towards lesser z and the magnitude of the negative velocity increases.

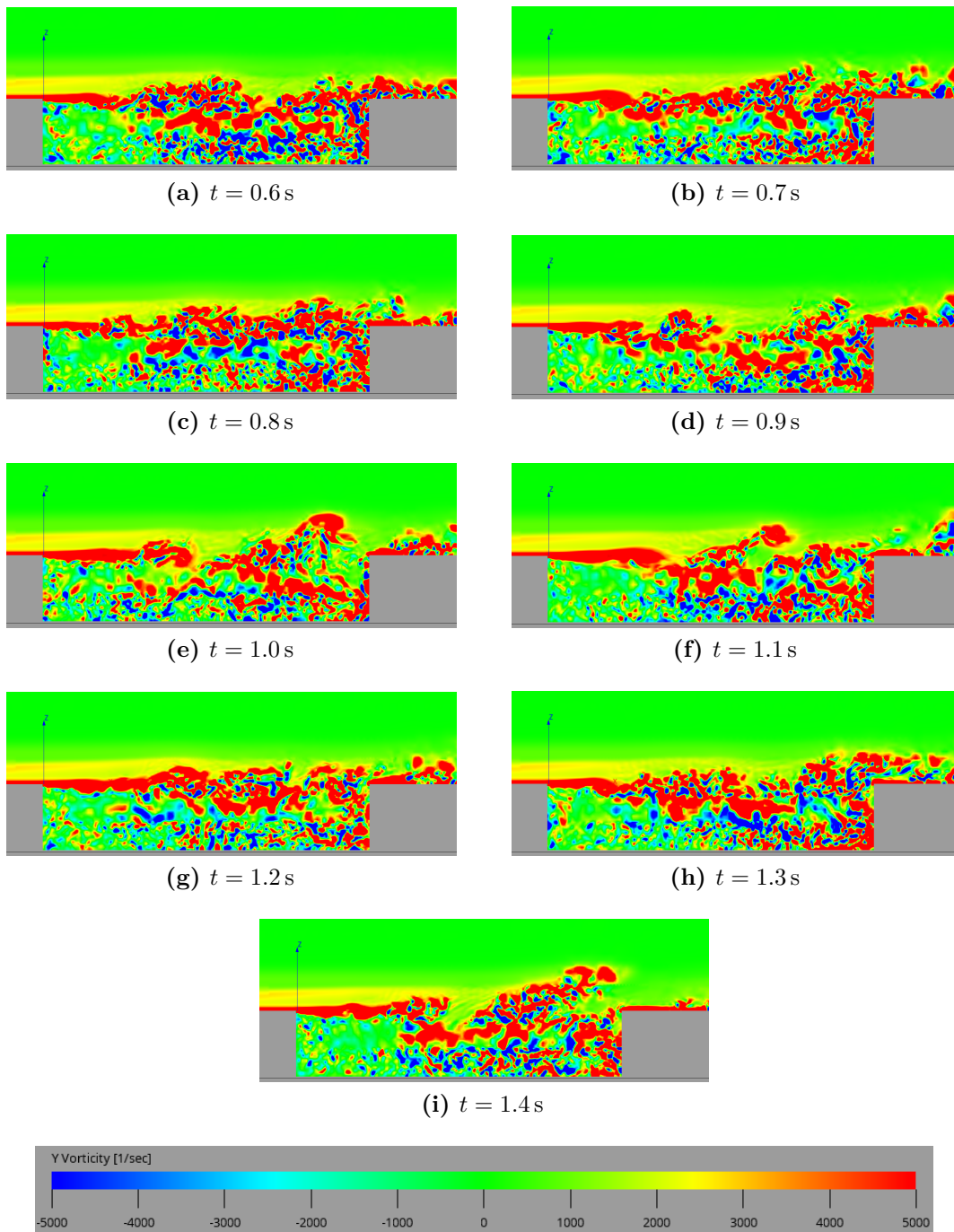


Figure 3.9: Vorticity ω_y evolution in a mid-span plane.

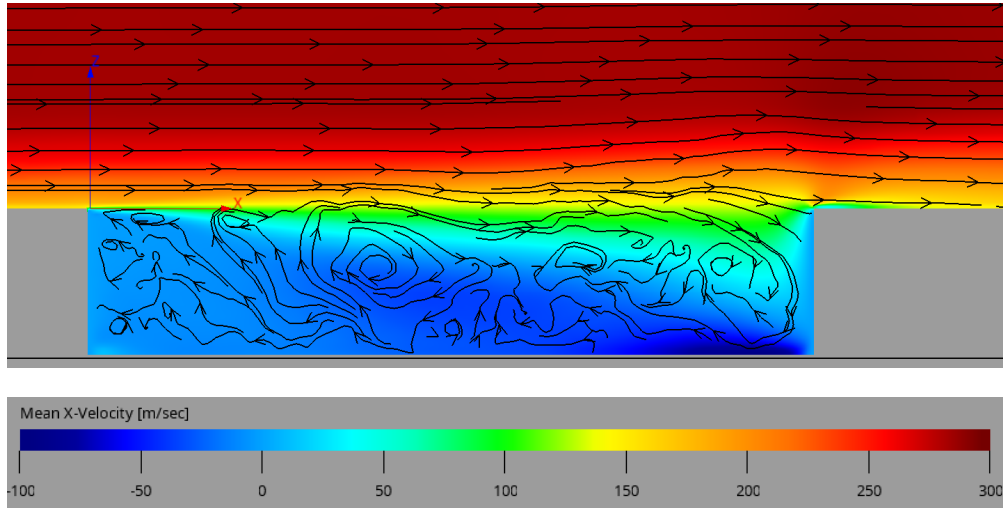


Figure 3.10: Streamlines in a mid-span plane, at $t = 1.4$ s, superimposed over the mean streamwise velocity U .

Turbulent Kinetic Energy

Figure 3.12 reports, together with the average streamwise velocity, the variances of the three velocity components: the streamwise u , the spanwise v and the vertical w . Mathematically, the variance of the streamwise velocity u is defined as

$$\sigma_u^2 = \frac{1}{T} \int_0^T (u(t) - \bar{u})^2 dt \quad (3.2)$$

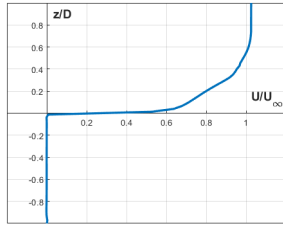
But the difference between the instantaneous velocity u and the average velocity $U = \bar{u}$ is the turbulent component of velocity u' in the Reynolds decomposition, so the variance of u is $\sigma_u^2 = \overline{u'^2}$. And similarly for $\overline{v'^2}$ and $\overline{w'^2}$.

Therefore, the variances of the velocities are associated with the turbulent kinetic energy TKE , which is defined as:

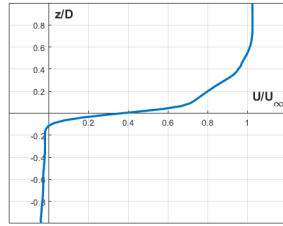
$$TKE = \overline{u'^2} + \overline{v'^2} + \overline{w'^2} \quad (3.3)$$

The plots show how the turbulent energy is concentrated in the shear layer and in the recirculation zone, and in the boundary layer downstream of the cavity.

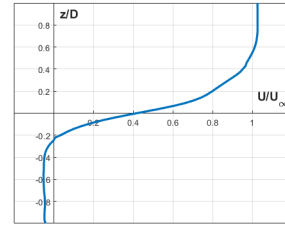
For the same positions of the velocity profiles, the profiles of the turbulent kinetic energy have been calculated, which are shown in Figure 3.13. The TKE peak is located near the shear layer, and its intensity increases in x . The only exception is the front lip, where the turbulent energy peak is located inside the cavity, whose intensity is, however, an order of magnitude lower than the energy peaks downstream.



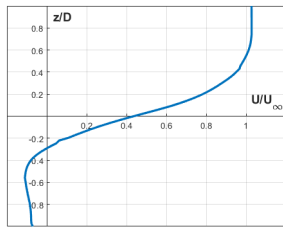
(a) $x = 0$ in (Front Edge)



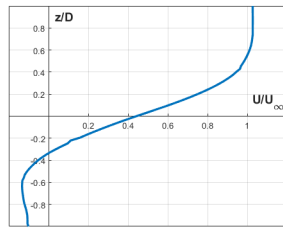
(b) $x = 2.5$ in



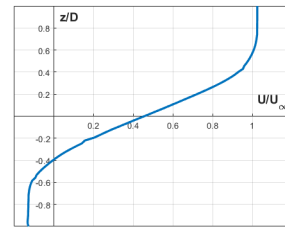
(c) $x = 5$ in



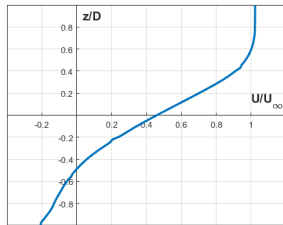
(d) $x = 7.5$ in



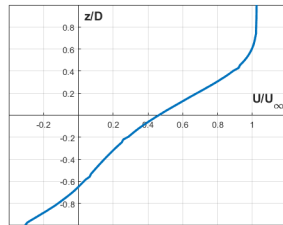
(e) $x = 10$ in



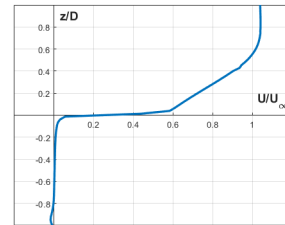
(f) $x = 12.5$ in



(g) $x = 15$ in



(h) $x = 17.5$ in



(i) $x = 20$ in (Rear Edge)

Figure 3.11: Mean streamwise velocity profiles for different positions along the cavity.

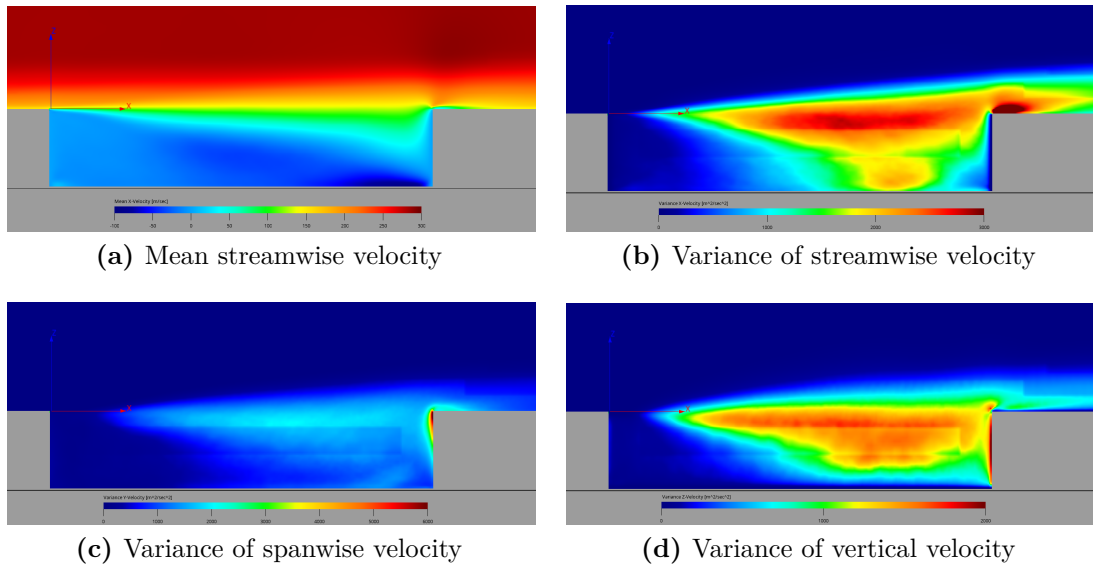


Figure 3.12: Mean streamwise velocity and variance of velocity components in a mid-span plane.

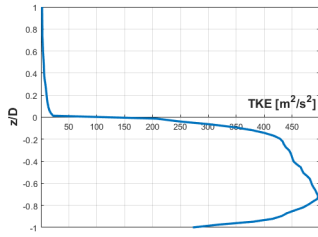
Planes Comparison

Subsequently, the data relating to the three acquisition planes have been compared to verify that the phenomenon were predominantly longitudinal, as described in Chapter 1.

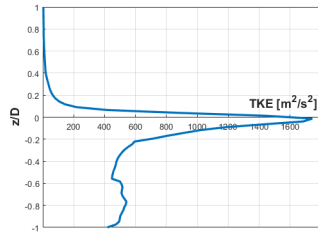
In Figure 3.15 the static pressure fields are reported. The three distributions differ slightly from each other, confirming what was said; however, some differences are still present. This is because, although the test rig is centred with respect to the wind tunnel, the cavity is eccentric, and in particular displaced by 1 inch towards the positive y . From the same plots it is also possible to note the passage from the high pressure area near the cavity rear wall to the low pressure area next to it, which is at the basis of the recirculation bubble formation.

The same comparison has been made with the streamwise velocities, in Figure 3.16, whose plots have been superimposed in Figure 3.14: the height and shape of the boundary layer is almost invariable along the span, while a greater variation is observed in the reverse flow zone.

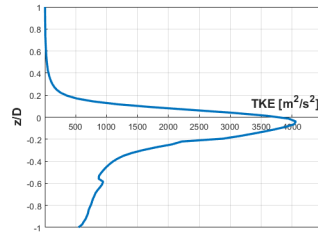
A further comparison has been made on the vertical velocity w , to verify the presence of edge effects. Figure 3.18 reports the mean vertical velocity W for the three planes. In it, in the second half of the cavity, a positive vertical velocity can be observed for negative y and vice versa: therefore, it is reasonable to assume that there is a recirculation bubble also in the spanwise plane, like in the streamwise plane. This is confirmed by the plot of the average spanwise velocity V for the plane



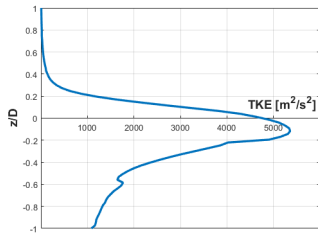
(a) $x = 0$ in (Front Edge)



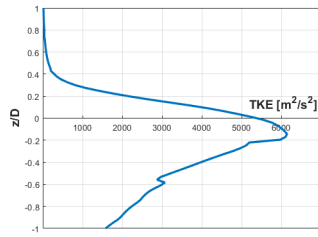
(b) $x = 2.5$ in



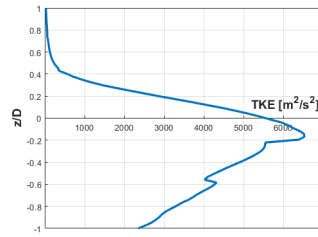
(c) $x = 5$ in



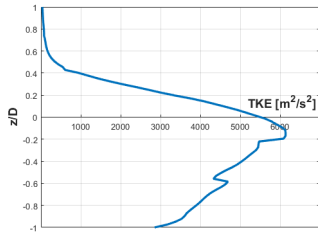
(d) $x = 7.5$ in



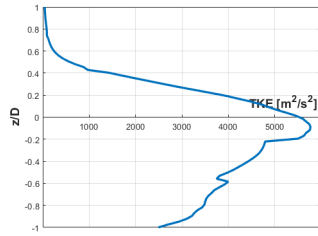
(e) $x = 10$ in



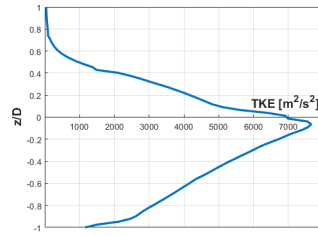
(f) $x = 12.5$ in



(g) $x = 15$ in



(h) $x = 17.5$ in



(i) $x = 20$ in (Rear Edge)

Figure 3.13: *TKE* for different positions along the cavity.

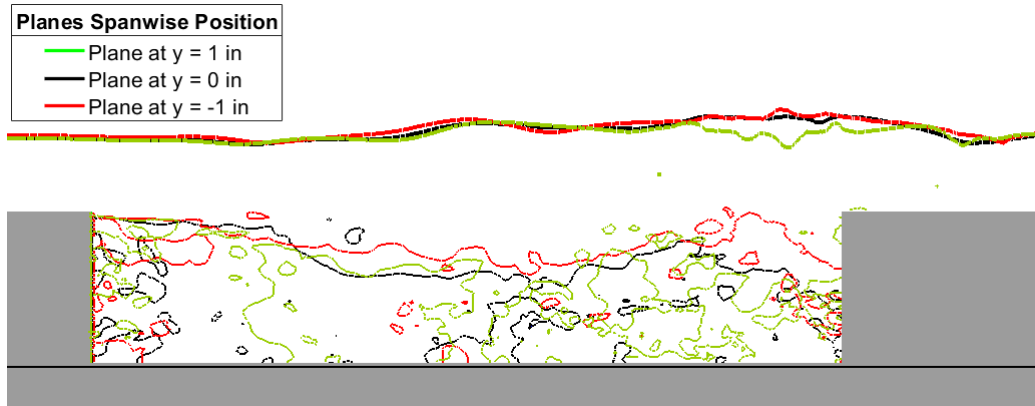


Figure 3.14: Boundary layer and reverse flow region comparison.

at $y = 0$, in Figure 3.17, where, in the second half of the cavity, there is a negative mean velocity on the bottom and a positive mean velocity near the shear layer. Therefore, also in the plane (y, z) there is a recirculation, but counter-clockwise.

Finally, in Figures 3.19 and 3.20 the variances of the streamwise velocity and the vertical velocity for the three planes are reported, respectively. There are some variations in the intensity of the turbulent velocity components, but not in the area where they are concentrated.

These data are summarized in Figure 3.21, which reports the mean streamwise velocity, mean vertical velocity, pressure and turbulent kinetic energy profiles for three different positions along the cavity, namely the front edge ($x = 0$ in), mid-length ($x = 10$ in) and the rear edge ($x = 20$ in).

The streamwise velocity profiles are almost perfectly coincident, as are those of TKE and pressure, with the only exceptions of the turbulent energy at the front edge and the pressure at the rear edge. The vertical velocity, instead, presents greater differences between the three planes.

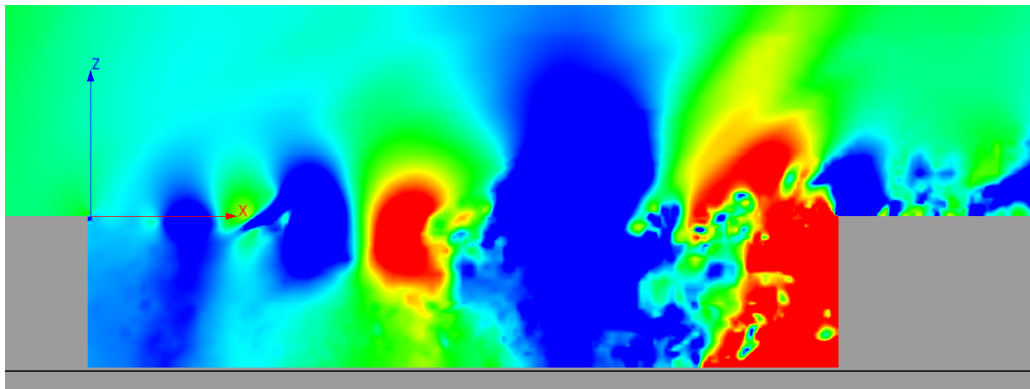
Pressure Oscillations

Locally, the pressure oscillations have been valued as Overall Sound Pressure Level (OASPL) and Sound Pressure Level (SPL); in particular, the OASPL has been computed along the entire cavity, while the SPL on two probes, the k22 and the k29.

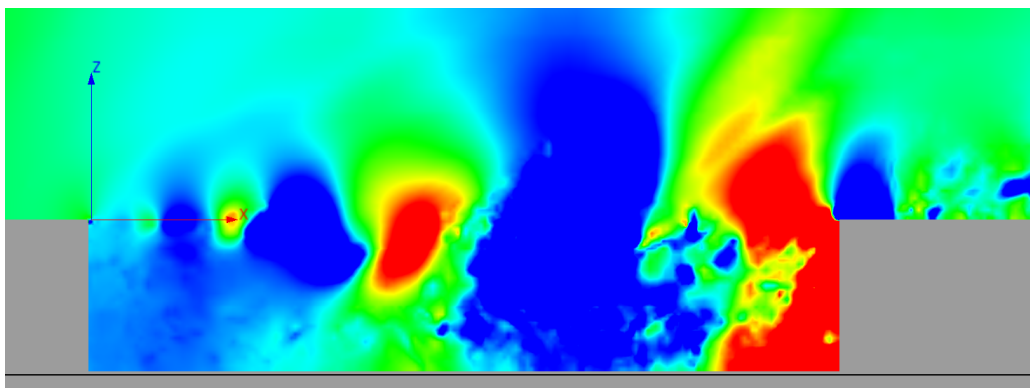
The OASPL is defined as:

$$OASPL = 20 \log_{10} \left(\frac{p'_{rms}}{p_{ref}} \right) \quad (3.4)$$

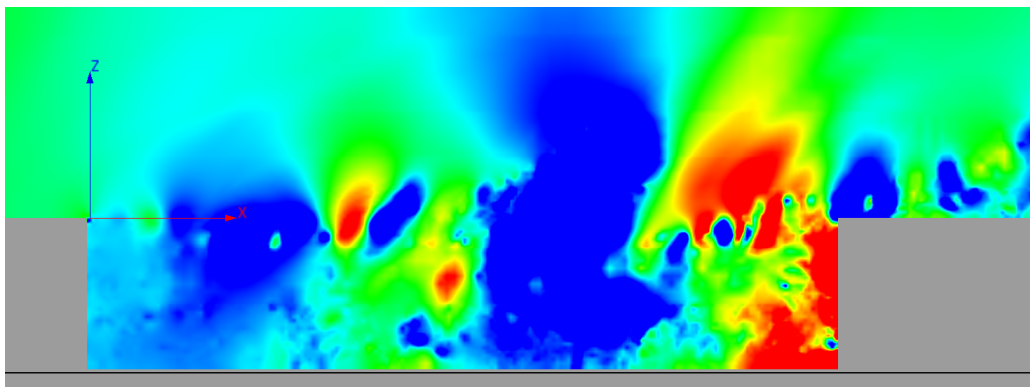
where the subscript rms denotes the root mean square of the pressure fluctuations p' , i.e. the difference between the instantaneous pressure p and the mean pressure



(a) Plane at $y = 1$ in



(b) Plane at $y = 0$ in (Mid-span plane)



(c) Plane at $y = -1$ in

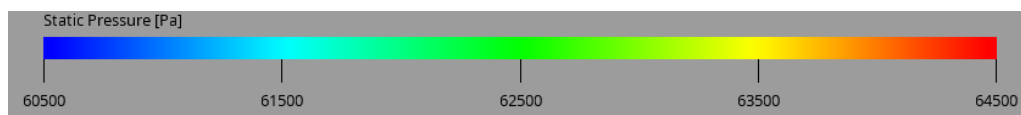
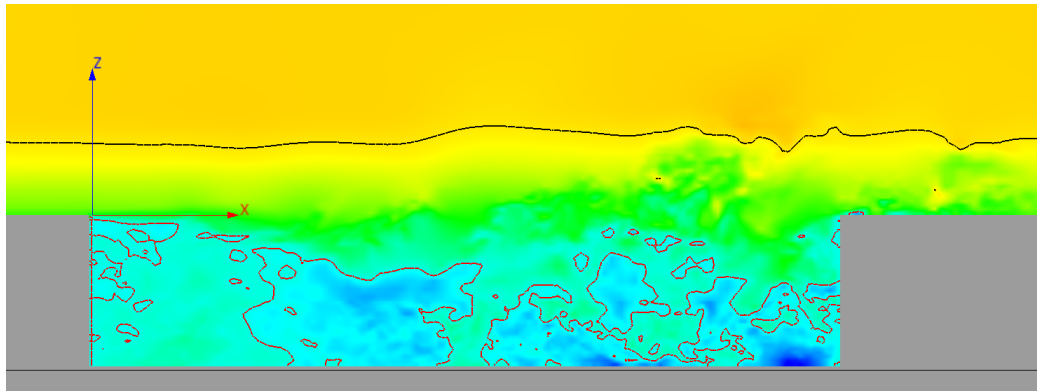
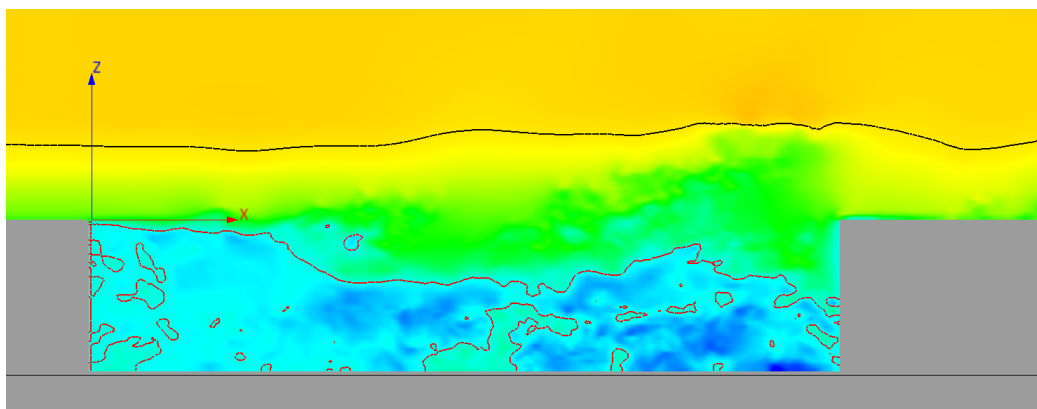


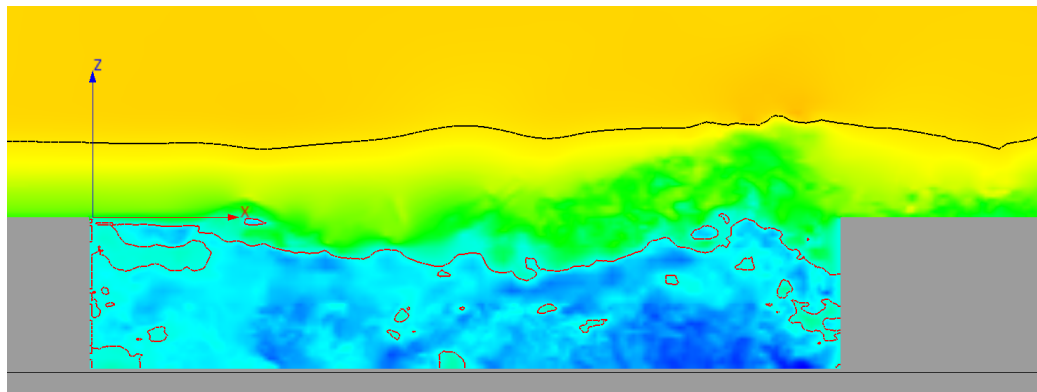
Figure 3.15: Static pressure p for three different y -normal planes, at $t = 1.4$ s.



(a) Plane at $y = 1$ in



(b) Plane at $y = 0$ in (Mid-span plane)



(c) Plane at $y = -1$ in

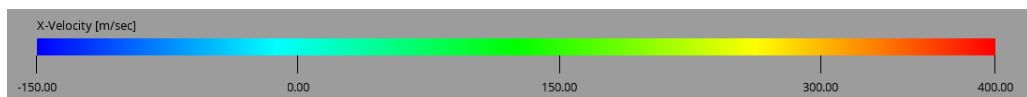


Figure 3.16: Streamwise velocities u for three different y -normal planes, at $t = 1.4$ s.

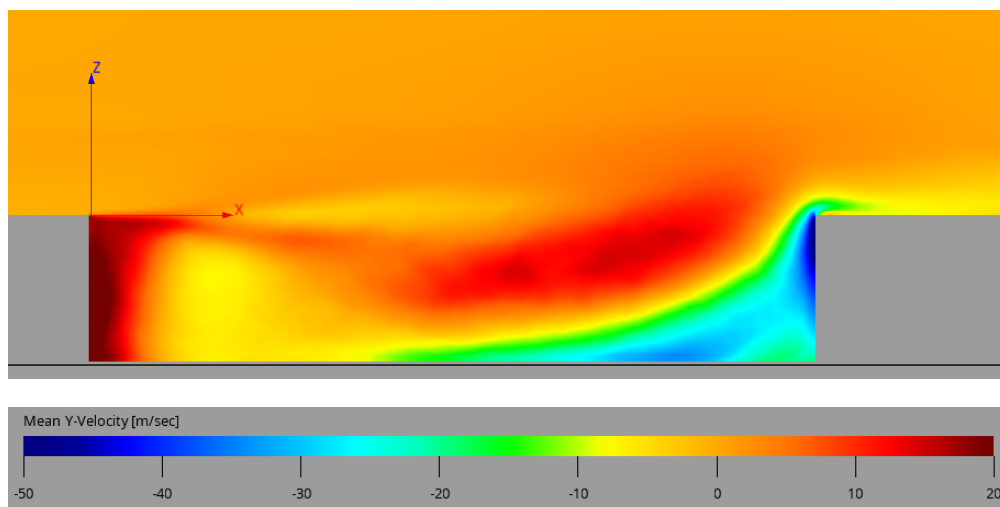


Figure 3.17: Mean spanwise velocity V in a mid-span plane.

p_{mean} , whose r.m.s. is:

$$p'_{rms} = \sqrt{\frac{1}{T} \int_{t_0}^{t_0+T} (p(t) - p_{\text{mean}})^2 dt} \quad (3.5)$$

while the reference pressure is $p_{ref} = 20 \mu\text{Pa}$.

The SPL, instead, is calculated as:

$$SPL = 20 \log_{10} \left(\frac{PSD}{p_{ref}^2} \right) \quad (3.6)$$

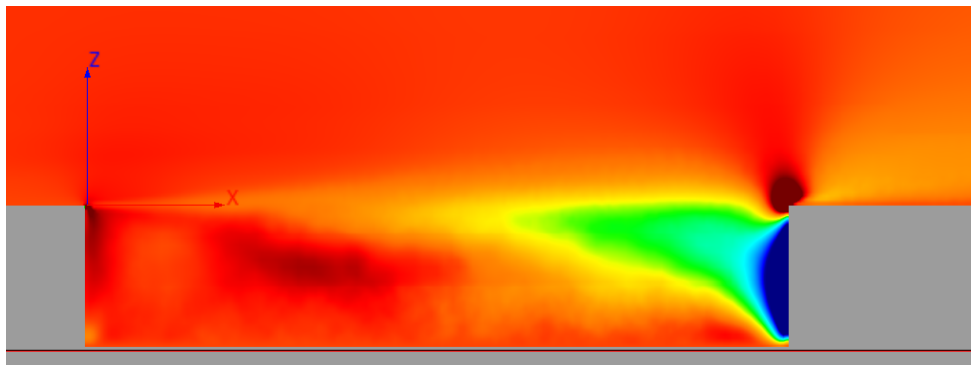
where the Power Spectral Density (PSD) is computed by the MATLAB function *pwelch*, dividing the signal in 16 segments, with an overlap of 50%.

Refinement Cases

The results obtained from the two simulations are compared with the experimental results[6], to verify whether convergence is achieved by refining the grid.

In Figure 3.22 the OASPL is depicted. Numerical results differ from the experimental ones by a factor of about 1.5 in p'_{rms} for all probes: this is probably due to an error in the case preparation or in the data post processing phase, that could not have been detected. However, the reported trend appears to be correct, meaning that if the error is located and resolved, the data numerical should converge to the experimental ones.

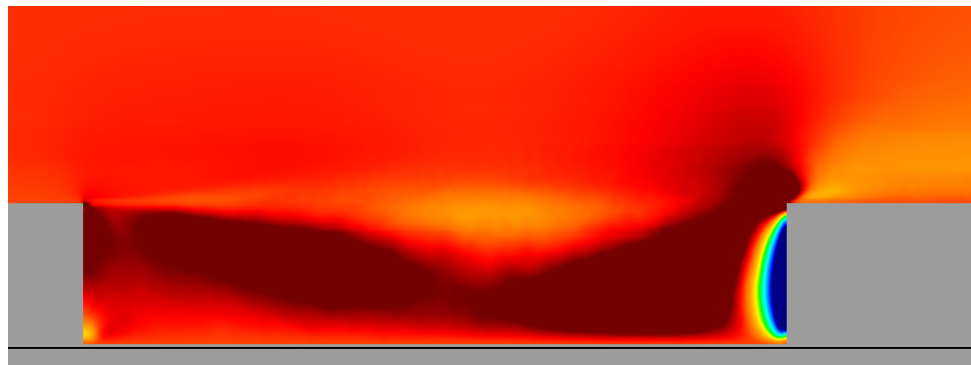
In Figure 3.23, instead, the SPL of the two probes k22 and k29 is reported. The spectra are in 1/12 octave band, i.e. the frequency domain has been divided



(a) Plane at $y = 1$ in



(b) Plane at $y = 0$ in (Mid-span plane)



(c) Plane at $y = -1$ in

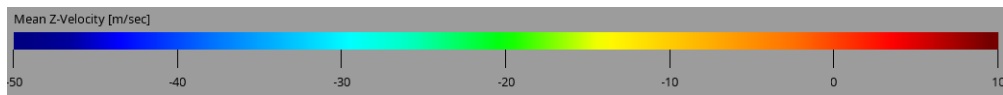
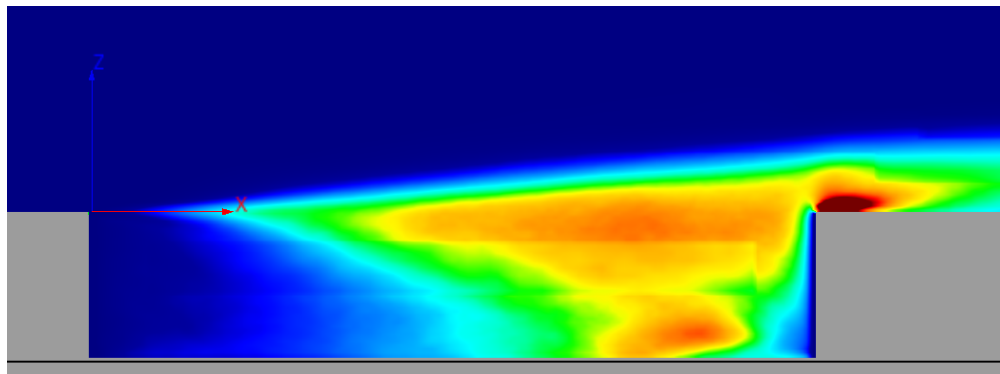
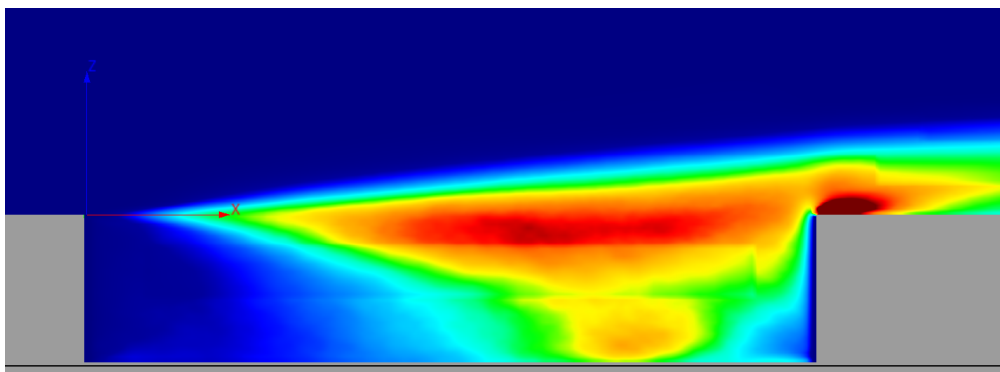


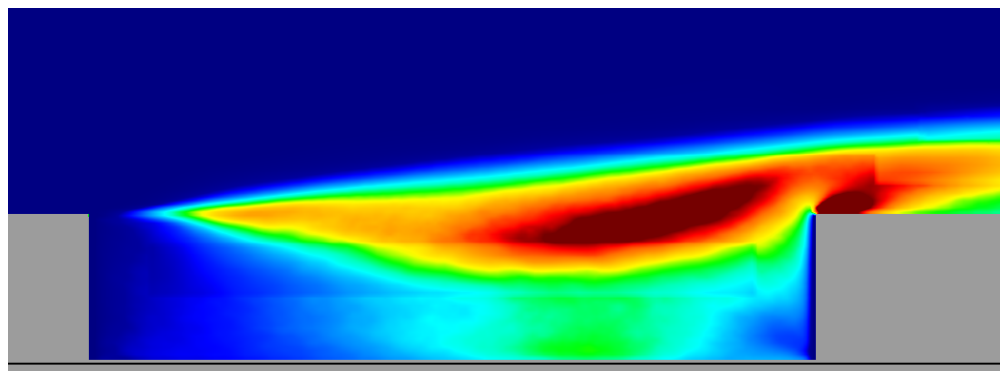
Figure 3.18: Mean vertical velocity W for three different y -normal planes.



(a) Plane at $y = 1$ in



(b) Plane at $y = 0$ in (Mid-span plane)



(c) Plane at $y = -1$ in

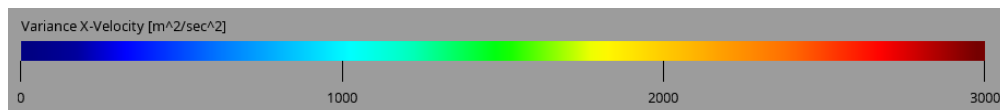
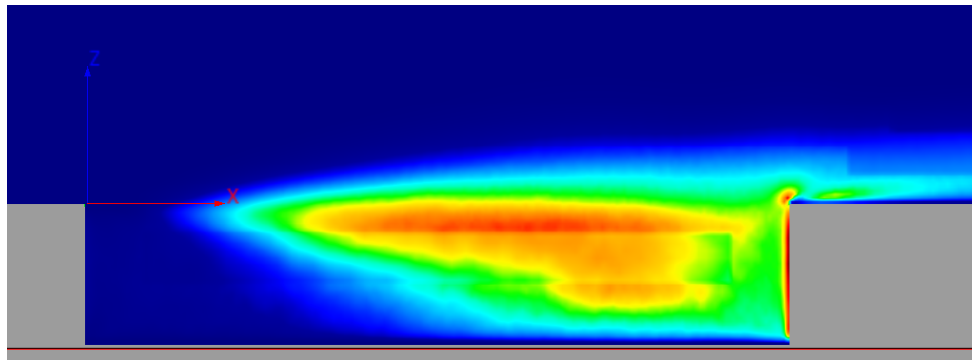
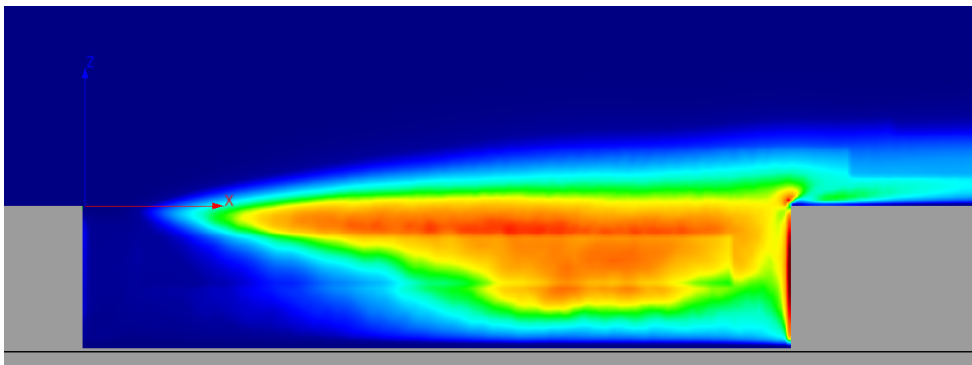


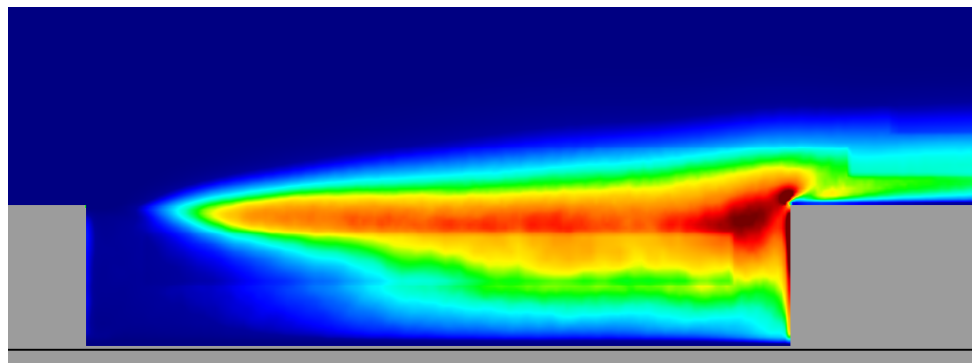
Figure 3.19: Variance of streamwise velocity $\overline{u'^2}$ for three different y -normal planes.



(a) Plane at $y = 1$ in



(b) Plane at $y = 0$ in (Mid-span plane)



(c) Plane at $y = -1$ in

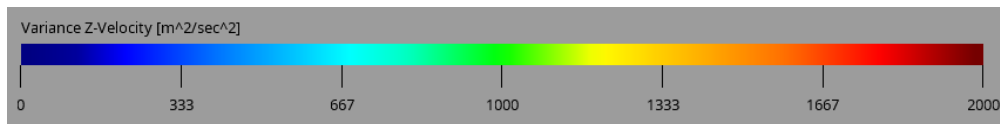
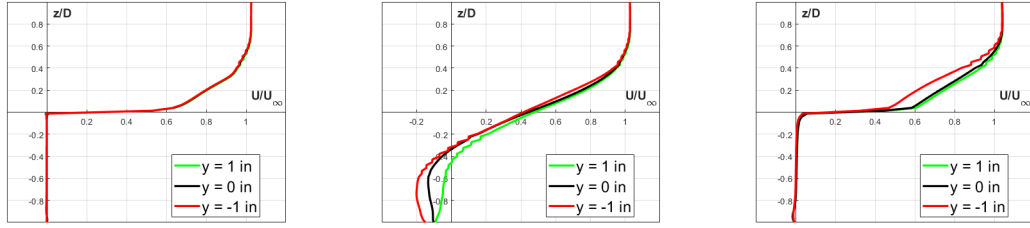
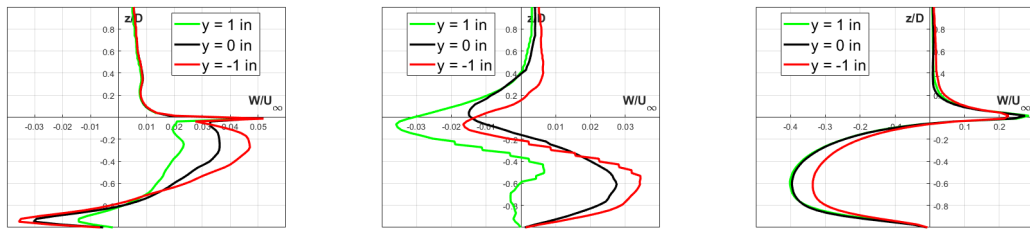


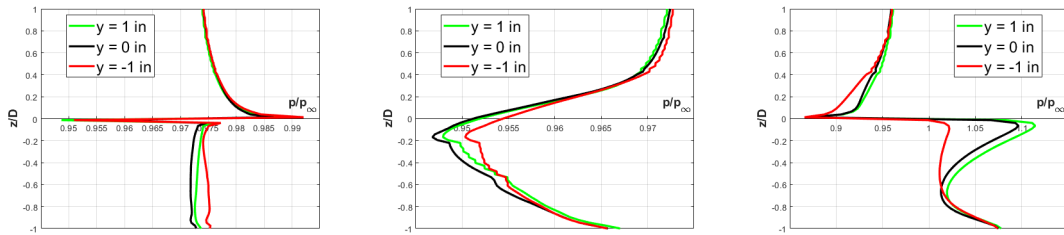
Figure 3.20: Variance of vertical velocity $\overline{w'^2}$ for three different y -normal planes.



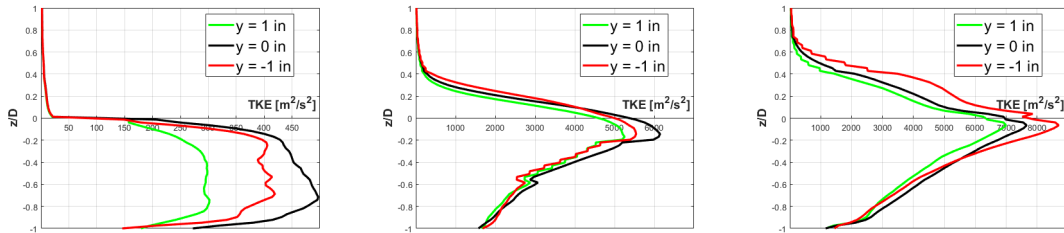
(a) Mean streamwise velocity at $x = 0$ in (b) Mean streamwise velocity at $x = 10$ in (c) Mean streamwise velocity at $x = 20$ in



(d) Mean vertical velocity at $x = 0$ in (e) Mean vertical velocity at $x = 10$ in (f) Mean vertical velocity at $x = 20$ in



(g) Static pressure at $x = 0$ in (h) Static pressure at $x = 10$ in (i) Static pressure at $x = 20$ in



(j) TKE at $x = 0$ in (k) TKE at $x = 10$ in (l) TKE at $x = 20$ in

Figure 3.21: U , W , p and TKE comparison between three planes.

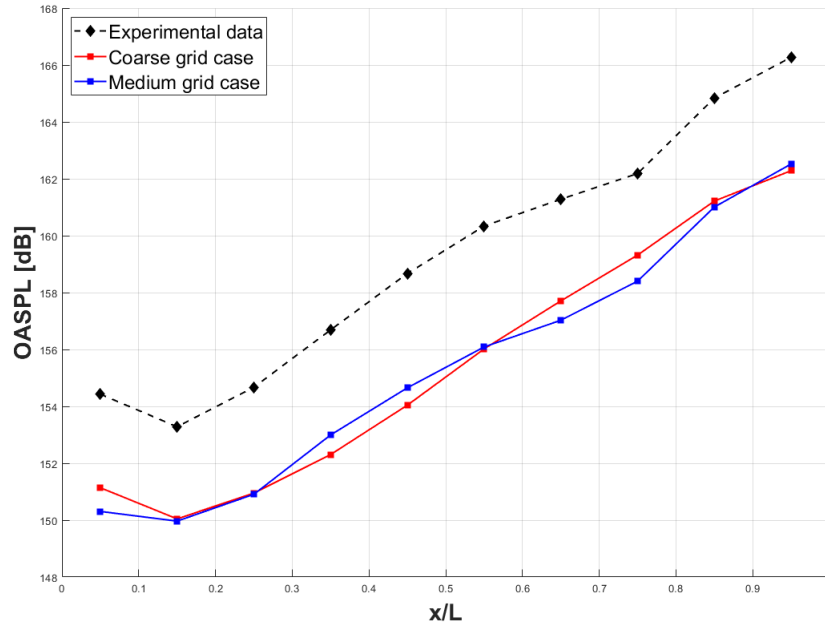


Figure 3.22: OASPL along the cavity with different grid resolution.

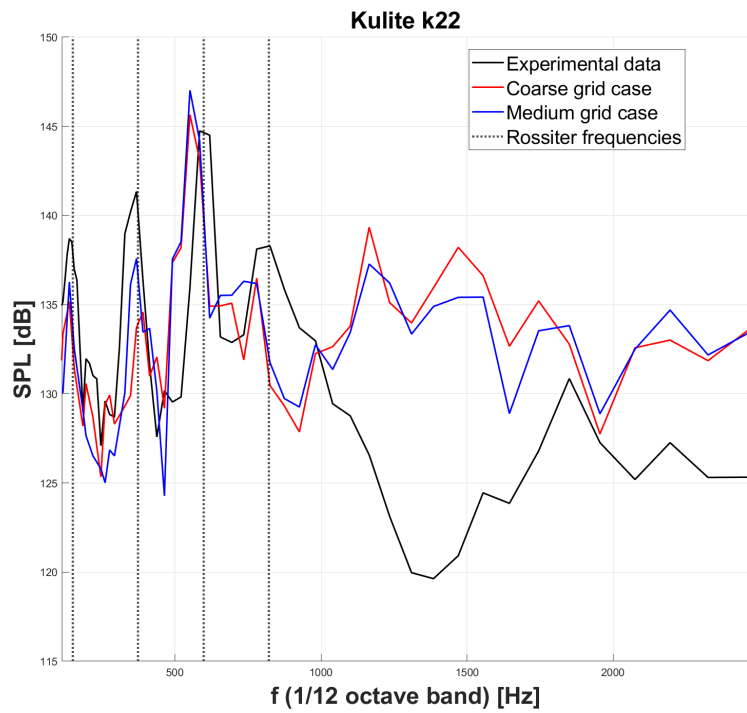
into intervals, in which the upper limit is $2^{\frac{1}{12}}$ times the lower limit, and the values are integrated on that interval.

From the spectra it is possible to note that for the low frequencies the numerical and experimental results are in agreement, while at the higher frequencies the oscillations are overestimated: in part this may be due to the failure to reach the temporal convergence, which causes broadband pressure oscillations to be higher.

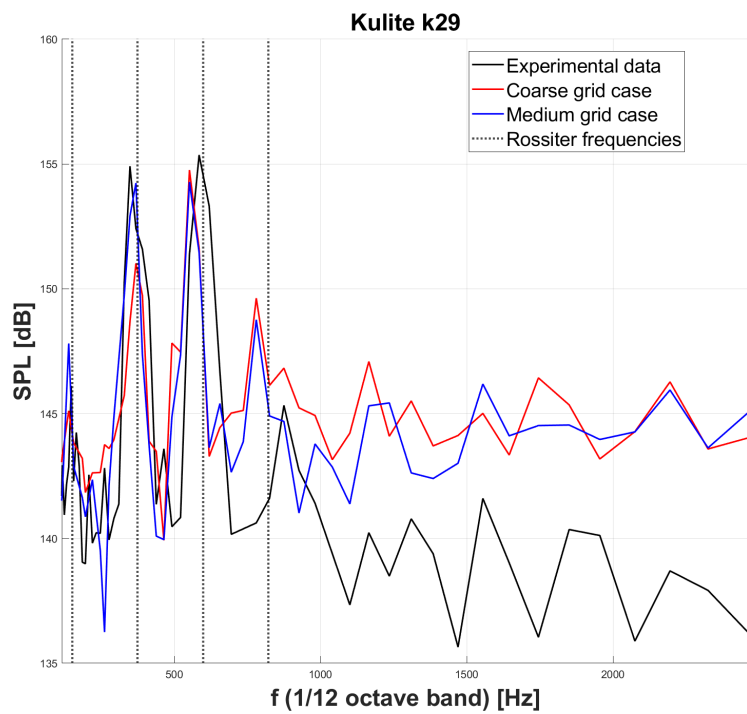
As said at the beginning of this section, being the cavity an open cavity flow, there are strong tonal components (the peaks in the spectra), which allow to identify the Rossiter frequencies. The latter are reported in the Table 3.6 on page 51 and compared with those measured by Henshaw[6] and the theoretical ones, according to the equation (1.8) on page 7, which in the graph are reported as dotted lines. The first two frequencies are correctly predicted, while the third and fourth are anticipated.

Comparison with Literature Data

Then, the results obtained have been compared with those present in the literature, and in particular with the results obtained by Nilsson[13], based on Delayed Detached Eddy Simulation (DDES) and Improved Delayed Detached Eddy Simulation (IDDES) methods, and those of Mancini[10], based instead on the same

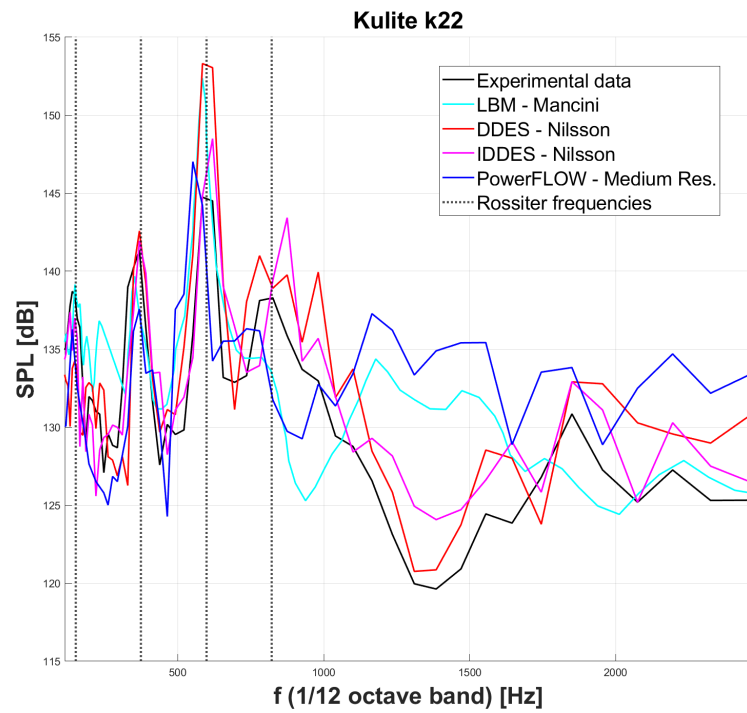


(a) k22

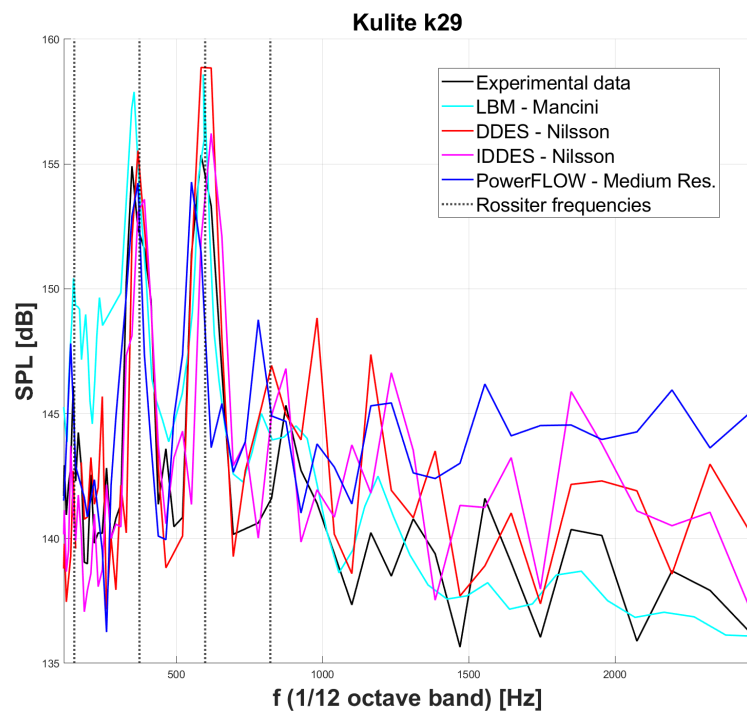


(b) k29

Figure 3.23: SPL at two probes with different grid resolution.



(a) k22



(b) k29

Figure 3.24: SPL at two probes with different numerical methods.

Table 3.6: Rossiter frequencies [Hz].

	Equation (1.8)	Measured[6]	Coarse grid case	Medium grid case
f_1	151	139	139	139
f_2	374	369	391	369
f_3	598	585	552	552
f_4	822	826	780	780

LBM and obtained through the same software. Ideally, the data obtained from the simulations performed should coincide with Mancini’s ones, however – as said before – there are some errors that cause our results to differ.

Figure 3.25 contains the OASPL, while Figure 3.24 shows the spectra. The most accurate method for predicting the OASPL is the IDDES. Furthermore, from the spectra, it can be seen that Mancini’s results also differ from the experimental ones, a sign that the LBM is less effective in predicting broadband components of pressure oscillations.

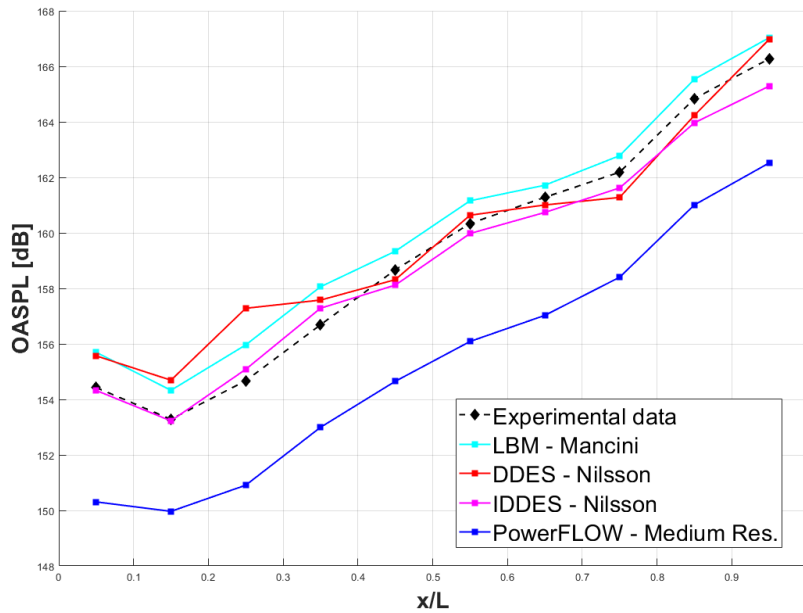


Figure 3.25: OASPL along the cavity with different numerical methods.

Chapter 4

Summary

The study of cavity flow, due to its numerous applications, remains of vital importance, and modern CFD techniques contribute to a better understanding of the phenomenon.

Among these, the Lattice-Boltzmann Method has been described in this paper and used, through the PowerFLOW software, to analyse the M219 cavity, comparing the numerical results with the experimental data collected by Henshaw and other numerical data present in the literature, obtained with different methods.

Three different simulations have been carried out, with an increasingly finer grid. The third of these, however, could not have been concluded.

The analysis observed how the boundary layer separated from the front edge reattaches downstream of the cavity, confirming the open-flow cavity behaviour suggested by the length-to-depth and width-to-depth ratios. Furthermore, through the streamlines, the recirculation bubble in the cavity itself was observed.

A comparison of several physical quantities on three different planes along the span then highlighted the presence of a recirculation bubble also in a span-aligned plane.

Finally, the pressure oscillations were analysed in terms of OASPL and SPL, identifying the Rossiter frequencies. The difference with respect to the experimental data hints the presence of a numerical error in the case preparation or in the post-processing phase, which however has not been identified. However, the trend seems to be in line with the experimental one. Finally, the comparison with the literature data shows that the most accurate method is DDES, and that a certain error in the broadband components is intrinsic in LBM. However, the PowerFLOW software has the advantage of a quasi-automatic generation of the grid, without the need for manual refinement near the walls, and a fully parametrizable case preparation, which allows changes without the need to recreate the model from scratch. Finally, the very nature of Lattice-Boltzmann Method lends itself to running simulations on multi-core platforms, such as the Politecnico's HPC.

Bibliography

- [1] D. Casalino, I. Gonzales-Martino, and S. Mancini. ‘On the Rossiter-Heller frequency of resonant cavities’. In: *Aerospace Science and Technology* 131 (Nov. 2022).
- [2] S. Chen and G.D. Doolen. ‘Lattice Boltzmann Method for Fluid Flows’. In: *Annual Review of Fluid Mechanics* 30 (June 1998).
- [3] C.O.L. Hamilton Smith, N. Lawson, and G.A. Vio. ‘History, review and summary of the cavity flow phenomena’. In: *European Journal of Mechanics/B Fluids* 108 (July 2024).
- [4] H.H. Heller and D. Bliss. ‘The physical mechanism of flow-induced pressure fluctuations in cavities and concepts for their suppression’. In: 2nd Aeronautics Conference. Hampton (VA), USA, 1975.
- [5] H.H. Heller, D.G. Holmes, and E.E. Covert. ‘Flow induced pressure oscillations in shallow cavities’. In: *Journal of Sound and Vibration* 18 (4) (1971).
- [6] M.J.d.C. Henshaw. *Verification and Validation Data for Computational Unsteady Aerodynamics*. M219 cavity case. British Aerospace (Operations) Ltd., Military Aircraft and Aerostructures, 2000.
- [7] D. Herrmann. *A Study of the Suitability of PowerFLOW as an Educational Engineering Design Tool for Undergraduate Students*. Center for Aerospace - Structures, University of Colorado.
- [8] K. Krishnamurty. *Acoustic radiation of two-dimensional rectangular cutouts in aerodynamics surfaces*. Technical Note 3487. NACA, Aug. 1955.
- [9] S.J. Lawson and G.N. Barakos. ‘Review of numerical simulations for high-speed, turbulent cavity flows’. In: *Progress in Aerospace Sciences* 47 (2011).
- [10] S. Mancini, A. Kolb, I. Gonzales-Martino, and D. Casalino. ‘Predicting high-speed feedback mechanism in rectangular cavities using lattice-Boltzmann very-large eddy simulations’. In: *Aerospace Science and Technology* 117 (June 2021).

BIBLIOGRAPHY

- [11] S. Mancini, A. Kolb, and F. Mayer. ‘Reducing aeroacoustic feedback mechanisms in rectangular cavity flows using passive modifications’. In: AIAA Aviation Forum. Virtual event, Aug. 2021.
- [12] B.T. Maureen, E.B. Plentovich, et al. *Cavity unsteady-pressure measurements at subsonic and transonic speed*. Technical Note 3669. NASA, 1997.
- [13] S. Nilsson, H. Yao, A. Karlsson, and S. Arvidson. ‘Effects of Aeroelastic Walls on the Aeroacoustics in Transonic Cavity Flow’. In: *Aerospace* 9 (Nov. 2022).
- [14] *PowerFLOW User’s Guide*. Dassault Systèmes. 2022.
- [15] A. Roshko. *Some measurements of flow in a rectangular cutout*. Technical Note 3488. NACA, Aug. 1955.
- [16] J.E. Rossiter. ‘Wind tunnel experiments of the flow over rectangular cavities at subsonic and transonic speeds’. In: *Aeronautical Research Council Reports and Memoranda* 3438 (Oct. 1964).
- [17] E. M. Vigen. ‘The lattice Boltzmann method: Fundamentals and acoustics’. PhD Thesis. Norwegian University of Science and Technology, Feb. 2014.
- [18] A. Wagner. ‘Theory and Applications of the Lattice Boltzmann Method’. PhD Thesis. University of Oxford, 1997.
- [19] A. Wagner. *A Practical Introduction to the Lattice Boltzmann Method*. Department of Physics, North Dakota State University, Aug. 2008.
- [20] HPC@POLITO website. URL: https://www.hpc.polito.it/legion_cluster.php.

Acronyms

CFD Computational Fluid Dynamics

DDES Delayed Detached Eddy Simulation

DES Detached Eddy Simulation

HPC High Performance Computing

IDDES Improved Delayed Detached Eddy Simulation

LBM Lattice-Boltzmann Method

LES Large Eddy Simulation

OASPL Overall Sound Pressure Level

PSD Power Spectral Density

RANS Reynolds-averaged Navier-Stokes

RHS Right Hand Side

r.m.s. root mean square

SPL Sound Pressure Level

URANS Unsteady RANS

VLES Very Large Eddy Simulation

VR Variable Resolution